Studies of Muon induced Background at the DoubleChooz Detector

Diplomarbeit
am Institut für Experimentalphysik
der Universität Hamburg

vorgelegt von
Thorsten Lammers

Februar 2008

Gutachter der Diplomarbeit

Prof. Dr. Caren Hagner
Prof. Dr. Dieter Horns

Abstract

In this diploma thesis, the impact of cosmic radiation on the background of the DoubleChooz Detector is studied. The Geant4-based Monte-Carlo simulation software package DOGS, that was installed from scratch, is used in order to obtain results on the energy depositions of muon induced secondary electrons, photons and neutrons in the different detector areas. The investigations provide statements on the linear correlation between deposited energy and production of photoelectrons in the scintillator and on the effects of photomultiplier positioning. Furthermore, progress is made on determining the rate of fast neutrons which can mimic the neutrino signal in the target region.

Kurzfassung

In der vorliegenden Diplomarbeit wird der Beitrag kosmischer Myonen zum Untergrund des DoubleChooz Detektors untersucht. Das auf Geant4 basierende Software Paket für Monte-Carlo Simulationen DOGS wurde von Grund auf installiert und benutzt, um Energiedepositionen in verschiedenen Detektorbereichen zu simulieren, die ihren Ursprung in Myon-induzierten Sekundärteilchen wie Elektronen, Photonen und Neutronen haben. Die Ergebnisse beinhalten Aussagen über den linearen Zusammenhang von Energiedeposition und Produktion von Photoelektronen im Szintillator, so wie über Effekte der Anordnung der Photomultiplier. Desweiteren werden Fortschritte in der Bestimmung einer Rate von schnellen Neutronen gemacht, welche in der Lage sind, die Signatur eines Neutrinoevents im Target zu erzeugen.

Contents

List of Figures

List of Tables

Chapter 1

Introduction

The Standard Model of particle physics (SM) describes elementary particles and their interactions. It is a relativistic quantum field theory that is consistent with many experimental results. Although phenomenons like neutrino oscillations have highlighted that the SM is not a complete theory and that it can be subject to expansions, it is a strong groundwork for particle physics. Three of the four existing fundamental interactions are part of the SM:[1]

- **Strong interaction**
  In the scope of particle physics, the strong interaction is the most powerful of the four fundamental forces. It is mediated by gluons and takes effect on quarks, antiquarks and gluons themselves. In Quantum chromodynamics (QCD), quarks and gluons are assigned to different colour and anticolour charges. Real particles have to fulfil the condition of being colour neutral which can be achieved by combination of three colours (baryons) or one colour and the corresponding anticolour (mesons). It has not been achieved yet to isolate colour charged particles. The force between a pair of quark and antiquark increases with the distance between them. This effect, called confinement, is the reason for the short range of the strong interaction.[2] At a certain distance the generation of a new quark-antiquark pair becomes energetically more favourable than further stretching of the bond between quark and antiquark.

[1] The gravitational force is not regarded in the SM. While it plays an important role in astrophysical dimensions, its effect on particles is negligible compared to the other forces.

[2] It can be explained by the fact that the mediators of the strong interaction, the gluons, carry colour charge themselves.

- **Weak interaction**
  The mediators of the weak interaction are the two charged bosons (W^+, W^-) with a mass of 80.4 GeV and the uncharged Z-boson with a mass of 91.2 GeV. Their high masses are the reason for the short range of the force, smaller than the diameter of an atomic nucleus. The weak interaction affects all particles, quarks and leptons. It is the only force in the SM that couples on neutrinos. Also it is responsible for the β-decay that is of special interest for the DoubleChooz experiment. Similar to the oscillations of neutrino mass eigenstates, the weak interaction allows quarks to do flavour changes which is described in the CKM-formalism.

- **Electromagnetic interaction**
  The characteristics of the electromagnetic interaction are specified in Quantum electrodynamics (QED). It describes the force between charged particles that is mediated by the uncharged and massless photon. Electromagnetic interactions are responsible for the attractive force between protons and electrons which can therefore form atoms. The electromagnetic interactions is the only force in the SM that has an infinite range. It unites the classical theories of electricity and magnetism into one theory.[3]

The particles involved in the SM are six quarks and six leptons that are categorised into 3 families of corresponding particles with different charge (see Table 1.1). The families differ in the mass of their particles. Antiparticles are sorted in the same way but with opposite charges [2].

Charge	Quarks
$\binom{+2/3}{-1/3}$	$\binom{u}{d}\binom{c}{s}\binom{t}{b}$
Charge	**Leptons**
$\binom{\pm 0}{-1}$	$\binom{\nu_e}{e}\binom{\nu_\mu}{\mu}\binom{\nu_\tau}{\tau}$

Table 1.1: Particles in the Standard Model

While the neutrino masses are set to zero in the SM, recent experiments have confirmed the existence of neutrino oscillations which implies a non-

[3]The weak and the electromagnetic interactions can then be seen as two peculiarities of the same electroweak force at low energies [1].

vanishing neutrino mass. The discovery of neutrino oscillations therefore results in the necessity to expand the SM by additional neutrino parameters (see Section 2). The search for such parameters is an important branch of today's particle physics. A deeper understanding of the mixing probabilites between the three different neutrino flavours is the driving force for the development of experiments like DoubleChooz. Due to the extremely low interaction probabilities of neutrinos, their detection requires an experimental setup with highest sensitivity. An understanding of background of any kind and its effective reduction is indispensable. In this context the present work tries to contribute to the comprehension of muon induced backgrounds at the DoubleChooz detector sites.

Further details on the behaviour of neutrinos in and beyond the SM and on important experiments from neutrino discovery to the observation of oscillations are provided in the following Chapter 2.
Chapter 3 then deals with the concept of the DoubleChooz experiment. The detection principle as well as the detector design are explained and some remarks are made on the importance of understanding cosmological backgrounds.
In Chapter 4 the simulation and software environment is mentioned before the studies on muon induced backgrounds are presented in Chapter 5. After some general surveys on the detector response and on the photomultiplier positioning, the particular risk potentials of electrons, photons and neutrons are analysed.
Then a summary of the results and a motivation for further research is given in Chapter 6.
Appendix A finally provides a short guideline for the used simulation and analysis software.

Chapter 2

Neutrino Physics and Cosmic Background

The neutrino is a neutral particle that belongs to the family of leptons. In the SM it appears in three flavour generations. In weak charged current processes (exchange of a charged W-boson), neutrinos and their charged counterparts of the same generation can merge into each other.[1]

$$\begin{pmatrix}\nu_e\\ e\end{pmatrix} \quad \begin{pmatrix}\nu_\mu\\ \mu\end{pmatrix} \quad \begin{pmatrix}\nu_\tau\\ \tau\end{pmatrix}. \tag{2.1}$$

Also the lepton generations differ in the mass of the charged leptons. The neutrino mass was long assumed to be 0 (and still is in the SM). However, recent experimental results show that neutrinos have a very small mass. Until now, only limits of this mass and the mass differences between neutrinos of different generations are known. The existence of a non-zero neutrino mass is a prerequisite for the appearence of neutrino oscillations (see Section 2.1). Being a fermion, the neutrino has a spin of 1/2 and negative chirality. Neutrinos are subject to the weak force only.[2] Due to their very low interaction rates with matter, neutrinos are able to pass through matter with nearly no disturbance. This makes them very difficult to detect and demands a precise knowledge of backgrounds in neutrino detection experiments. Neutrinos are created in different types of particle reactions. Two examples are the production of ν_e in the sun and the β-decay $n \to p + e^- + \bar{\nu}_e$ [3].

[1] The same classification applies for antiparticles in an analogue way.

[2] They are also subject to the gravitational force that affects all particles in the SM, but is extremely weak and can be neglected in this context.

This chapter deals with a theoretical and experimental phenomenology of neutrino physics in the context of DoubleChooz as a reactor neutrino experiment. For this, the third neutrino mixing angle θ_{13} is of special importance. In the following sections the phenomenon of neutrino flavour oscillations is explained. Some earlier experiments are described that did important preliminary work for DoubleChooz. At the end, cosmic radiation is described with a special focus on fast neutron production.

2.1 Neutrino Oscillations and Mixing

Analoguous to the CKM formalism[3] that describes quark mixing, neutrinos are subject to flavour oscillations. This quantum mechanical phenomenon describes transitions between different neutrino flavours $\nu_\alpha \leftrightarrow \nu_\beta$ $(\alpha, \beta = e, \mu, \tau)$[4]. The following facts are crucial for the description of neutrino oscillations:

- While the total lepton number L is conserved, Lepton flavour numbers L_α are not strictly conserved. Neutrino flavours can mix.[4]
- For the existence of neutrino ocsillations, it is a requirement that not all neutrinos are massless and that neutrino masses are different.

The second point is an extension to the simple SM where neutrinos are assumed to be massless. Therefore, neutrino oscillations are not described in the SM. A mixing between neutrino mass and flavour eigenstates provides the base principle for oscillations. It has been observed by different solar and atmospheric neutrino experiments (see Section 2.2). Formally, this mixing can be described as a number n of neutrino flavour eigenstates $|\nu_\alpha\rangle$ with $\langle\nu_\beta|\nu_\alpha\rangle = \delta_{\alpha\beta}$ that are a superposition of n neutrino mass eigenstates $|\nu_i\rangle$ with $\langle\nu_j|\nu_i\rangle = \delta_{ij}$ and vice versa. The orthonormal eigenstates are linked via a unitary mixing matrix U [5].[5] For 3-flavour oscillations, this matrix is fully written in Section 2.1.2.

$$|\nu_\alpha\rangle = \sum_i^n U_{\alpha i}|\nu_i\rangle, \quad |\nu_i\rangle = \sum_\alpha^n (U^+)_{i\alpha}|\nu_\alpha\rangle = \sum_\alpha^n U^*_{\alpha i}|\nu_\alpha\rangle \tag{2.2}$$

[3]Named after **C**abibbo, **K**obayashi, and **M**askawa.

[4]Conservation of L is not the case for Majorana particles ($\nu_\alpha = \bar{\nu}_\alpha$).

[5]The matrix is called *MNS*-Matrix (**M**aki-**N**akagawa-**S**akata matrix). If it was the identity matrix, flavour and mass eigenstates would be the same.

with

$$UU^+ = 1, \quad \text{i.e.} \quad \sum_i^n U_{\alpha i} U_{i\beta}^* = \delta_{\alpha\beta}, \quad \sum_\alpha^n U_{\alpha i} U_{j\alpha}^* = \delta_{ij}, \tag{2.3}$$

where U^+ is the adjoint matrix to U.
An interacting neutrino ν_α creates a charged lepton l_α of the same flavour α (ν_e yields an e, ν_μ a μ, and ν_τ a τ) [6]. In the case of an antineutrino $U_{\alpha i}$ transforms to $U_{\alpha i}^*$ so that

$$|\bar{\nu}_\alpha\rangle = \sum_i^n U_{i\alpha}^* |\bar{\nu}_i\rangle. \tag{2.4}$$

A unitary $n \times n$ matrix has n^2 parameters and $2n$ neutrino states with $2n-1$ relative phases. These phases can be determined so that $(n-1)^2$ independent parameters remain. The $\frac{1}{2}n(n-1)$ weak mixing angles of an n-dimensional rotation matrix combined with $\frac{1}{2}(n-1)(n-2)$ CP-violating phases are normally chosen as the independent parameters [4].[6] In its rest frame the stationary mass eigenstates $|\nu_i\rangle$ with $i = 1, ..., n$ obey the Schrödinger equation

$$i\frac{\partial}{\partial \tau_i}|\nu_i(\tau_i)\rangle = E_i|\nu_i(\tau_i)\rangle, \tag{2.5}$$

applying the convention $\hbar = c = 1$. τ_i and E_i are time and energy of the neutrino in its rest frame. The equation is solved by

$$|\nu_i(\tau_i)\rangle = e^{-iE_i\tau_i}|\nu_i(0)\rangle \tag{2.6}$$

for the time development of a neutrino mass eigenstate $|\nu_i\rangle$. Hence, a pure neutrino flavour eigenstate $|\nu_\alpha\rangle = \sum_i^n U_{\alpha i}|\nu_i\rangle$ will develop with time to

$$|\nu(\tau_i)\rangle = \sum_i^n U_{\alpha i} e^{-iE_i\tau_i}|\nu_i\rangle = \sum_i^n U_{\alpha i} U_{\beta i}^* e^{-iE_i\tau_i}|\nu_\beta\rangle. \tag{2.7}$$

Here, the last term includes the amplitude for an oscillation $\alpha \to \beta$ at the eigentime τ_i:

$$A(\alpha \to \beta; t) = \sum_i^n U_{\alpha i} U_{\beta i}^* e^{-iE_i\tau_i}. \tag{2.8}$$

$E_i\tau_i$ can be rewritten in laboratory-frame variables:

[6] See Section 2.1.2 for an example of U in three dimensions.

$$E_i\tau_i = E_i t - p_i L, \tag{2.9}$$

where L is the distance the neutrino travels between source and detection and t is the time that elapses during the trip. Both, L and t are defined by experimental parameters and common to all ν_i. Using $m_i^2 \ll E^2$ for relativistic energies, the momentum p_i can be approximated by

$$p_i = \sqrt{E^2 - m_i^2} \cong E - \frac{m_i^2}{2E} \tag{2.10}$$

so that

$$E_i\tau_i \cong E(t-l) + \frac{m_i^2}{2E}L. \tag{2.11}$$

Since $E(t-l)$ does not depend on the different mass eigenstates ν_i, it can be disregarded for the following observations concerning neutrino flavour transitions. With $L = ct$ $(c = 1)$, the flavour transition amplitude transforms to

$$A(\alpha \to \beta; t) = A(\alpha \to \beta; L) = \sum_i^n U_{\alpha i} U_{\beta i}^* e^{-i\frac{m_i^2}{2}\cdot\frac{L}{E}} \tag{2.12}$$

for neutrinos, and with (2.4)

$$A(\bar{\alpha} \to \bar{\beta}; t) = \sum_i^n U_{\alpha i}^* U_{\beta i} e^{-i\frac{m_i^2}{2}\cdot\frac{L}{E}} \tag{2.13}$$

for antineutrinos.
The probability P for neutrino flavour transitions depending on the observable parameters L, being the distance between source and the neutrino energy in vacuum E, can now be calculated:

$$\begin{aligned} P(\alpha \to \beta; t) &= |A(\alpha \to \beta; t)|^2 = \left| \sum_i^n U_{\alpha i} U_{\beta i}^* e^{-i\frac{m_i^2}{2}\cdot\frac{L}{E}} \right|^2 \\ &= \sum_{i,j}^n U_{\alpha i} U_{\alpha j}^* U_{\beta i}^* U_{\beta j} e^{-i\frac{\Delta m_{ij}^2}{2}\cdot\frac{L}{E}} \\ &= \sum_i^n |U_{\alpha i} U_{\beta i}^*|^2 + 2\Re \sum_{j>i} U_{\alpha i} U_{\alpha j}^* U_{\beta i}^* U_{\beta j} e^{-i\frac{\Delta m_{ij}^2}{2}\cdot\frac{L}{E}} \end{aligned} \tag{2.14}$$

with $\Delta m_{ij}^2 = m_i^2 - m_j^2$.
Assuming CP-invariance, which requires U to be real, (2.14) simplifies to:

$$P(\alpha \to \beta; t) = \delta_{\alpha\beta} - 4 \sum_{j>i} U_{\alpha i} U_{\alpha j} U_{\beta i} U_{\beta j} \sin^2 \left(\Delta m_{ij}^2 \frac{L}{4E} \right). \tag{2.15}$$

From (2.14) some conclusions can be drawn about the behaviour of neutrino oscillations:

- The probability of flavour change oscillates with L/E.
- The oscillation probabilities do not depend on the absolute values of the neutrino masses m_i, but only on a squared mass difference Δm_{ij}^2. Thus, oscillation experiments are not capable of determining neutrino masses. Only the relation between different mass eigenstates is accessible.
- The phenomenon of neutrino flavour oscillations does not change the total flux in a neutrino beam. Only the distribution of flavours in the beam is varied:
$$\sum_{\beta} P(\nu_\alpha \to \nu_\beta) = 1, \tag{2.16}$$
with β comprising all neutrino flavours.

2.1.1 The case of 2-flavour oscillations

For the special case of oscillations with only two neutrino flavours involved (eg. $\nu_e \leftrightarrow \nu_\mu$), equation (2.15) can be further simplified. Here, the transformation matrix U only includes the two mass eigenstates ν_1 and ν_2 and the two flavour eigenstates ν_α and ν_β and can be written as

$$\begin{pmatrix} |\nu_e\rangle \\ |\nu_\mu\rangle \end{pmatrix} = \begin{pmatrix} \cos\theta & \sin\theta \\ -\sin\theta & \cos\theta \end{pmatrix} \cdot \begin{pmatrix} |\nu_1\rangle \\ |\nu_2\rangle \end{pmatrix}.^{7} \tag{2.17}$$

This 2×2-matrix can be parameterized with only one mixing angle θ. Furthermore, there is only one mass difference $\Delta m^2 = m_2^2 - m_1^2$. For $\alpha \neq \beta$ it is now possible to write (2.15) as

[7] This is similar to the simplification to two quark flavours in the CKM-environment.

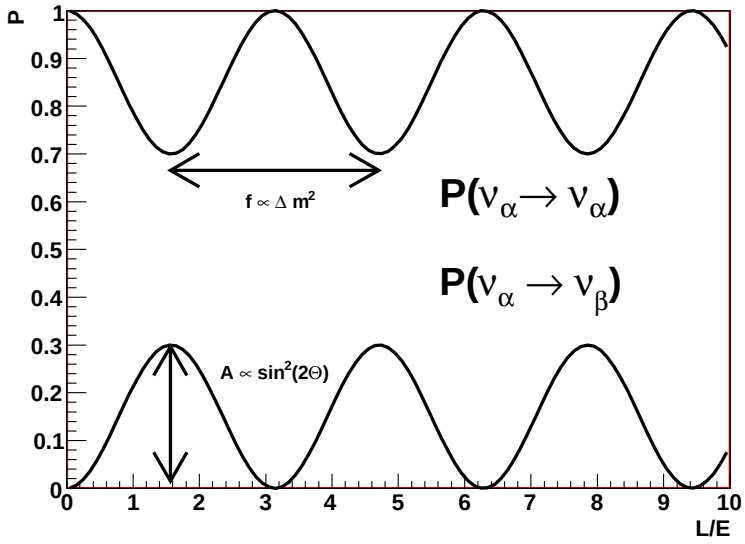

Figure 2.1: Schematic view of neutrino oscillations with 2 flavours for $\sin^2 2\theta = 0.3$. While the oscillation frequency f depends on the mass difference Δm, the oscillation amplitude A depends on the mixing angle θ.

$$P(\nu_\alpha \to \nu_\beta) = P(\bar{\nu}_\alpha \to \bar{\nu}_\beta) = \sin^2 2\theta \sin^2 \left(\Delta m^2 \frac{L}{4E}\right).^8 \tag{2.18}$$

This formula clearly demonstrates the fact that oscillations can only occur if ($\theta \neq 0 \wedge \Delta m^2 \neq 0$) is given. Thus, the value of θ controls the oscillation amplitude and the value of Δm^2 controls the oscillation frequency (see Figure 2.1). The 2-flavour formalism is applicable to many experiments that are not sensitive to effects of the third neutrino flavour due to measurement precision issues.[9]

2.1.2 The case of 3-flavour oscillations

According to the SM that deals with 3 neutrino flavours (ν_e, ν_μ, and ν_τ), a 3-flavour formalism with a 3×3-mixing matrix provides the complete description of neutrino mixing. The additional dimension results in more degrees

[8]There are no imaginary elements in U. Therefore, the transition probabilities turn out to be the same for neutrino and antineutrinos.

[9]DoubleChooz belongs to the first generation of high precision experiments that demand application of the full 3-flavour formalism.

of freedom. The mixing angle θ of the 2-flavour formalism is replaced by the three mixing angles θ_{12}, θ_{13}, and θ_{23}. In the same manner, two independent mass differences Δm_{ij} must now be considered.[10] The mixing matrix is usually parameterized in the following form:

$$\begin{aligned} U &= \begin{pmatrix} 1 & 0 & 0 \\ 0 & c_{23} & s_{23} \\ 0 & -s_{23} & c_{23} \end{pmatrix} \cdot \begin{pmatrix} c_{13} & 0 & s_{13}e^{-i\delta} \\ 0 & 1 & 0 \\ -s_{13}e^{i\delta} & 0 & c_{13} \end{pmatrix} \cdot \begin{pmatrix} c_{12} & s_{12} & 0 \\ -s_{12} & c_{12} & 0 \\ 0 & 0 & 1 \end{pmatrix} \\ &= \begin{pmatrix} c_{12}c_{13} & s_{12}c_{13} & s_{13}e^{-i\delta} \\ -s_{12}c_{23} - c_{12}s_{23}s_{13}e^{i\delta} & c_{12}c_{23} - s_{12}s_{23}s_{13}e^{i\delta} & s_{23}c_{13} \\ s_{12}s_{23} - c_{12}c_{23}s_{13}e^{i\delta} & -c_{12}s_{23} - s_{12}c_{23}s_{13}e^{i\delta} & c_{23}c_{13} \end{pmatrix} \end{aligned} \tag{2.19}$$

where $s_{ij} = \sin\theta_{ij}$ and $c_{ij} = \cos\theta_{ij}$. The CP-violating phase δ with $-\pi \leq \delta \leq \pi$ causes, if $\delta \neq 0$, the imaginary terms in U.[11] In the case of Majorana-neutrinos[12], there are two additional CP-violating phases. Those phases do not have influence on the oscillation and cannot be observed by oscillation experiments. Therefore, they are neglected in this context.

2.1.3 Experimental approach to the measurement of unknown parameters

There are two experimental solutions to the problem of finding the third mixing angle θ_{13} and the CP-violating phase δ. In the calculation of flavour transition probabilities for $n = 3$ at reactor neutrino experiments like DoubleChooz, the CP-violating phase dissappears in those terms that describe oscillations $\nu_\alpha \rightarrow \nu_\alpha$ with $\alpha = e, \mu, \tau$. Furthermore, matter effects can be disregarded for the experimental dimensions of L and the involved neutrino energies E_ν of some MeV.[13] DoubleChooz studies the $\bar{\nu}_e \rightarrow \bar{\nu}_e$-disappearance channel. The oscillation probability at DoubleChooz is

$$P_{\bar{\nu}_e \rightarrow \bar{\nu}_e} = 1 - \sin^2(2\theta_{13}) \sin^2(\Delta_{31}) - \alpha^2 \cos^4\theta_{13} \sin^2(2\theta_{12}), \tag{2.20}$$

[10] The relation $\Delta m^2_{23} = \Delta m^2_{13} - \Delta m^2_{12}$ makes one of the three terms dependent on the other two.

[11] As mentioned above, $\frac{1}{2}n(n-1)$ weak mixing angles and $\frac{1}{2}(n-1)(n-2)$ CP-violating phases give the parameters of an $n \times n$ mixing matrix. Thus, in the case of $n = 2$, no imaginary part is necessary while for $n = 3$ it has to be considered.

[12] $\nu_\alpha = \bar{\nu}_\alpha$

[13] For further information on matter effects see eg. [7].

with $\Delta_{31} = \frac{\Delta m^2_{31} L}{4E_\nu}$ and $\alpha = \frac{\Delta m^2_{21}}{\Delta m^2_{31}} \simeq 3 \cdot 10^{-2}$ [8].
The DoubleChooz detector design is not capable of providing information about the influences of CP-violation and matter effects [9]. This fact enhances the precision limits to the measurement of θ_{13} as it can be determined independently.[14] θ_{13} is the last unknown neutrino mixing angle and therefore of special interest for the international research community at the moment.

The superbeam experiments T2K and Noνa have a different approach. High energy accelerator neutrinos in the range of GeV are detected over a long baseline of several hundred kilometers. As opposed to DoubleChooz, their measurements will be influenced by θ_{13}, δ and matter effects. It will be very difficult to disentangle contributions of those parameters. A previous independent determination of θ_{13} by a reactor neutrino experiment would offer the opportunity for such experiments to identify the CP-violating phase δ as the last missing parameter in the mixing matrix. The possible CP-violation in the leptonic sector is considered to be a promising approach to explaining the matter-antimatter-asymmetry of the universe.

2.2 History of Neutrino Experiments

The existence of the neutrino was first postulated by Wolfgang Pauli in 1930 [10].[15] He was the first to interpret the β-decay as a three-particle phenomenon where the neutrino explains the continuous spectrum of the resulting electron and saves the conservation laws of energy and angular momentum. It took another 25 years until the Hanford-detector of Reines and Cowan experimentally confirmed the existence of the neutrino in 1956 [11]. Similar to DoubleChooz, they already used antielectron-neutrinos from a nuclear reactor in Hanford, USA, that were detected via inverse β-decay (see Section 3.2.1). In another important experiment, Wu et al. discovered Parity-violation in the weak interaction in 1957 [12]. One year later, Goldhaber et al. were able to directly determine the helicity of the electron-

[14] A dependence on Δm^2 remains. Its values are the main responsibles for the location of the first oscillation minimum. Deviations from the assumed values can result in the fact that the far detector location at $L = 1.05\,\text{km}$ is not exactly the oscillation minimum anymore.

[15] Pauli called it "neutron" at that time. It was re-named to neutrino when Chadwick found the "real" neutron two years later.

neutrino $H(\nu_e) = -1$ [13].[16]
Other experiments have already proven the existence of exactly three light neutrino-flavours (ν_e, ν_μ, ν_τ). After Ledermann et al. discovered the existence of a second neutrino flavour in 1962, the DONuT[17] experiment found the third neutrino ν_τ in 2000 [14] [15]. Eventually, the number of light[18] neutrino flavours could be determined as $N_\nu \simeq 3$ at LEP[19] with increasing accuracy from 1990 [16] [17] [18] [19].
There are now many experiments that study the phenomenon of neutrino oscillations. Here, the mixing angles, the mass differences, and a possible CP-violation play the most important roles. As neutrino sources, solar neutrinos are used as well as nuclear reactors and high energetic artificial neutrino beams from particle accelerators. It is distinguished between experiments that directly search for ν_β appearance in a pure ν_α-source[20], and experiments that use variations in the expected ν_α-flux as proof for flavour oscillations (disappearance-experiments). Two of those experiments particularly affected the motivation of DoubleChooz and will now be presented:

2.2.1 KamLAND

The **Kam**ioka **L**iquid Scintillator **An**tineutrino **D**etector situated in an underground laboratory in Japan, 1000 m below the surface (2800 m.w.e.[21]), was built to observe neutrino oscillations. KamLAND started taking data in 2002. It is a long baseline experiment that uses a liquid scintillator detector to study disappearance of electron antineutrinos that originate from nuclear reactors at different distances to the laboratory. 80 % of the neutrino flux arrives from 53 Japanese reactors within a distance of 140-210 km. In order to compensate the flux reduction that is due to this distance, a large detection volume is required. The target of 1 kton of ultra pure liquid scintillator is contained in a transparent nylon balloon that is surrounded by mineral oil inside a stainless steel vessel. The mineral oil has the function of a buffer against radioactive impurities of the photomultipliers. On the inner wall of

[16] The neutrino mass was assumed to be zero. A non vanishing neutrino-mass results in a helicity $H(\nu) > -1$.
[17] **D**irect **O**bservation of the **Nu** **T**au
[18] $m_\nu < m_Z/2$
[19] **L**arge-**E**lectron-**P**ositron-collider at CERN
[20] α, $\beta = e$, μ, τ and $\alpha \neq \beta$.
[21] meters of water equivalent

the steel vessel, 1879 photo multiplier tubes detect the neutrino signal via the typical delayed signal of an inverse beta-decay (see Section 3.2.1). As a muon veto, a water Cerenkov counter is built around the inner detector structure. The Cerenkov light is detected by another layer of Outer detector PMT's. A schematic drawing of the detector setup is shown in Figure 2.2 [20].
In 2003, first results reported a rate of neutrino events of

$$\frac{N_{Observed}}{N_{Expected}} = 0.611 \pm 0.085\,(\text{stat.}) \pm 0.041\,(\text{sys.})[21]. \tag{2.21}$$

Compared to other experiments with a shorter baseline, these observations clearly implied the presence of neutrino oscillations (see Figure 2.3). The results were confirmed with a bigger data sample in 2005 [22].
Furthermore, the shape of the additionally measured neutrino energy spectrum gives information about the reasons for the neutrino disappearance. In this way, the hypotheses of neutrino decay and decoherence could be confuted leaving neutrino oscillations as most probable explanation.[22] A fit to the energy spectrum also gives a precise value for the oscillation parameter Δm_{12}. Combined with the results of other solar neutrino experiments, the solar neutrino oscillation parameters are determined as

$$\Delta m_{12} = 8.0^{+0.6}_{-0.4} \times 10^{-5}\,\text{eV}^2 \qquad \theta_{12} = 33.9^{\circ}{}^{+2.4^{\circ}}_{-2.2^{\circ}}. \tag{2.22}$$

Thus, KamLAND confirmed that neutrino oscillations are the solution to the solar neutrino problem. Leaving θ_{13} as the only still unknown oscillation parameter, the success of KamLAND further motivated the development of another liquid scintillator reactor antineutrino experiment.[23] From a technical point of view, the KamLAND experiment proved that a liquid scintillator neutrino experiment with a long baseline in the range of several kilometers can be successful. The baseline of 1 km at DoubleChooz therefore seemed to be controllable.

[22] Refer to [23] for neutrino decay and to [24] for decoherence model.

[23] Super-Kamiokande [25] and K2K [26] had already found values for the atmospheric oscillation parameters being $\Delta m_{23} \simeq \Delta m_{13} = 2.4^{+0.6}_{-0.5} \times 10^{-3}\,\text{eV}^2$ and $\sin^2 2\theta_{23} = 0.40^{+0.10}_{-0.07}$.

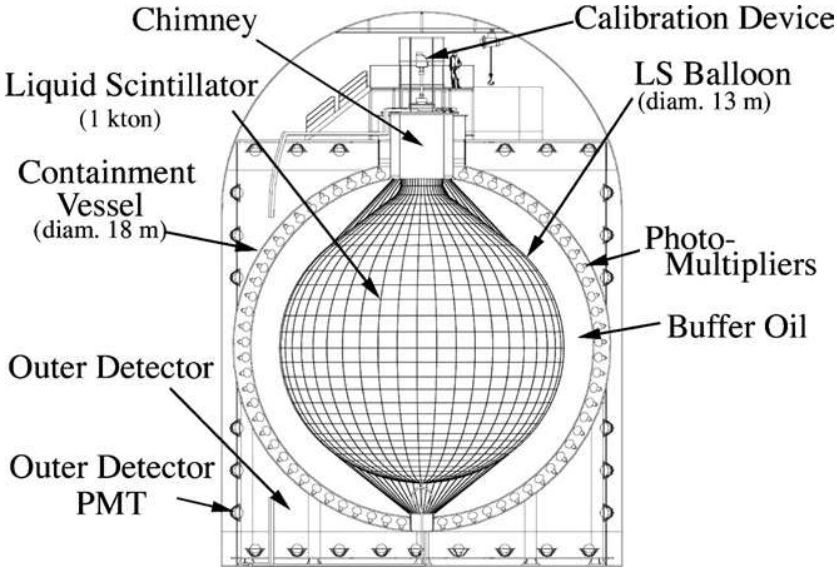

Figure 2.2: Schematic view of the KamLAND detector.

2.2.2 CHOOZ

The CHOOZ experiment is the direct predecessor to DoubleChooz [27]. It was performed between April 1997 and July 1998 with a single detector situated in an underground laboratory in about 1 km distance to two nuclear reactors at a depth of 300 m.w.e.[24] The flux of reactor antineutrinos ($\bar{\nu}_e$) was analyzed in order to find hints for neutrino oscillations. The original aim was to further describe and understand the oscillations detected at the Kamiokande experiment [28]. The "atmospheric neutrino anomaly", that was investigated at Kamiokande, describes the observation of a ν_μ/ν_e ratio that is only one half of the expectations. An explanation for this could be the oscillations $\nu_\mu \leftrightarrow \nu_\tau$ or $\nu_\mu \leftrightarrow \nu_e$. By measuring Δm^2 of equation (2.18) with a neutrino flux sensitivity known to better than 2 %, CHOOZ successfully removed the possibility of explaining the atmospheric neutrino anomaly by $\nu_\mu \leftrightarrow \nu_e$ (see Figure 2.4).[25] No oscillations $\nu_\mu \rightarrow \nu_e$ could be observed at CHOOZ. The measured ratio between expected and observed events was

$$R = 1.01 \pm 2.8\,\% \,(\text{stat.}) \pm 2.7\,\% \,(\text{sys.})[30]. \tag{2.23}$$

The mixing angle θ_{13} could therefore be limited to

[24] This laboratory is now used for the DoubleChooz far detector (see Section 3).
[25] Super-Kamiokande then finally proved the effect to be caused by $\nu_\mu \leftrightarrow \nu_\tau$ [29].

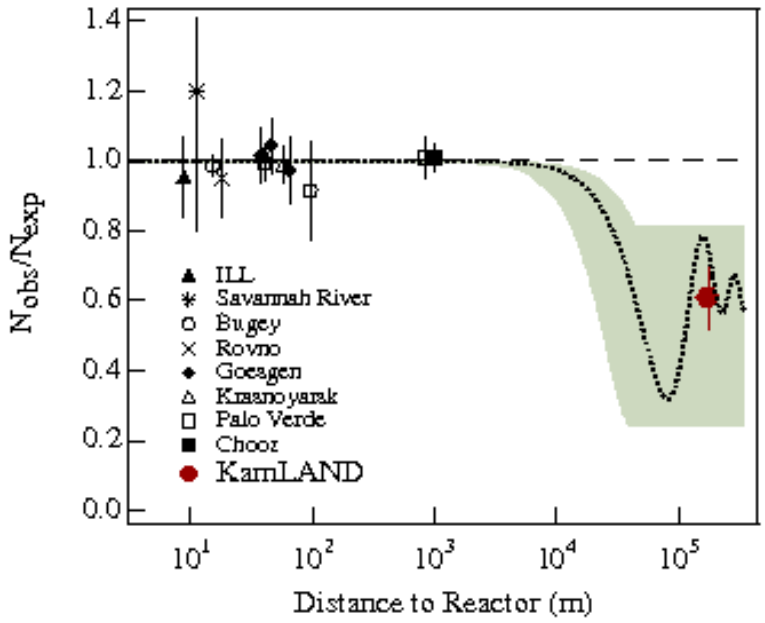

Figure 2.3: Ratios between observations and expectations of neutrino events at different reactor experiments. As first experiment, KamLAND shows a clear deviation from $N_{obs}/N_{exp} = 1$. For comparison a theoretical oscillation curve is included ($\sin^2 2\theta = 0.833$, $\Delta m^2 = 5.5 \times 10^{-5}\,\mathrm{eV}^2$) [21].

$$\sin^2 2\theta_{13} < 0.12\,(90\,\%\mathrm{CL}) \qquad \text{at}\,\Delta m^2_{13} \simeq 3 \times 10^{-3}\,\mathrm{eV}^2. \tag{2.24}$$

The CHOOZ experiment could find an upper limit of the third mixing angle θ_{13}. In order to continue the search for its exact value, the architecture of the CHOOZ detector had to be improved. This was a motivation for the development of the DoubleChooz experiment.
The main concept of the CHOOZ detector was taken as model for Double-Chooz (see Figure 2.5).
As detector, a cylindrical steel vessel with 5.5 m of diameter and heigth was placed into a cylindrical hole of 7 m diameter and heigth. The detector was surrounded by 0.75 m of low activity gravel shielding that was supposed to protect the detector from radioactivity originating in the rock. The detector itself consisted of:

- A 5-ton target of Gd-loaded scintillator.

- A 70 cm thick containment region for the purpose of catching gamma-radiation from neutron capture on Gd in the target. Also, it protected the target from radioactivity of the inner detector PMT's that were mounted on the outer wall of the containment region. It was filled with unloaded scintillator.

- A 80 cm thick veto region equipped with additional PMT's in order to reject backgrounds from cosmic muons. It was also filled with undoped scintillator.

Improvements of this setup at DoubleChooz will result in a signal-to-noise ratio increase by a factor of four. The target volume will be doubled and the containment region between target and PMT alignment will be split up into a non-scintillating buffer zone and a dedicated γ-catcher region [31]. Moreover, the gravel shielding will be replaced by a more efficient steel shielding. Due to its higher density, the steel shielding area can also be thinner, leaving a bigger volume for the detector. Another aspect that clarifies the importance of the CHOOZ experiences is an unpredicted behaviour of the Gd-loaded scintillator. Nitrates that were used to dissolve the Gd caused a reaction that coloured the scintillator. The running phase was therefore restricted. This observation gave reason to the development of a new, more stable scintillator which is currently done by the Max-Planck Institute in Heidelberg.

2.3 Muon-induced Background

The investigation of backgrounds in the DoubleChooz experiment deals with electrons, photons, and neutrons. Due to their high risk potential in terms of disturbing the neutrino signal, as will be discussed in Chapter 5, neutrons are of special interest. The background radiation that is studied in this work originates from interactions of high energetic muons in the steel and rock solids that surround the neutrino target area. Those muons are generated in air showers of cosmic radiation.
Cosmic particles have their source in energetic processes in the sun as well as in extrasolar events such as supernovae and neutron stars [32]. Of these particles, 90 % are protons, 9 % helium nuclei, and about 1 % electrons and heavier nuclei. The earth's atmosphere is permanently exposed to a flux of cosmic particles. It is varied by electromagnetic effects from the global

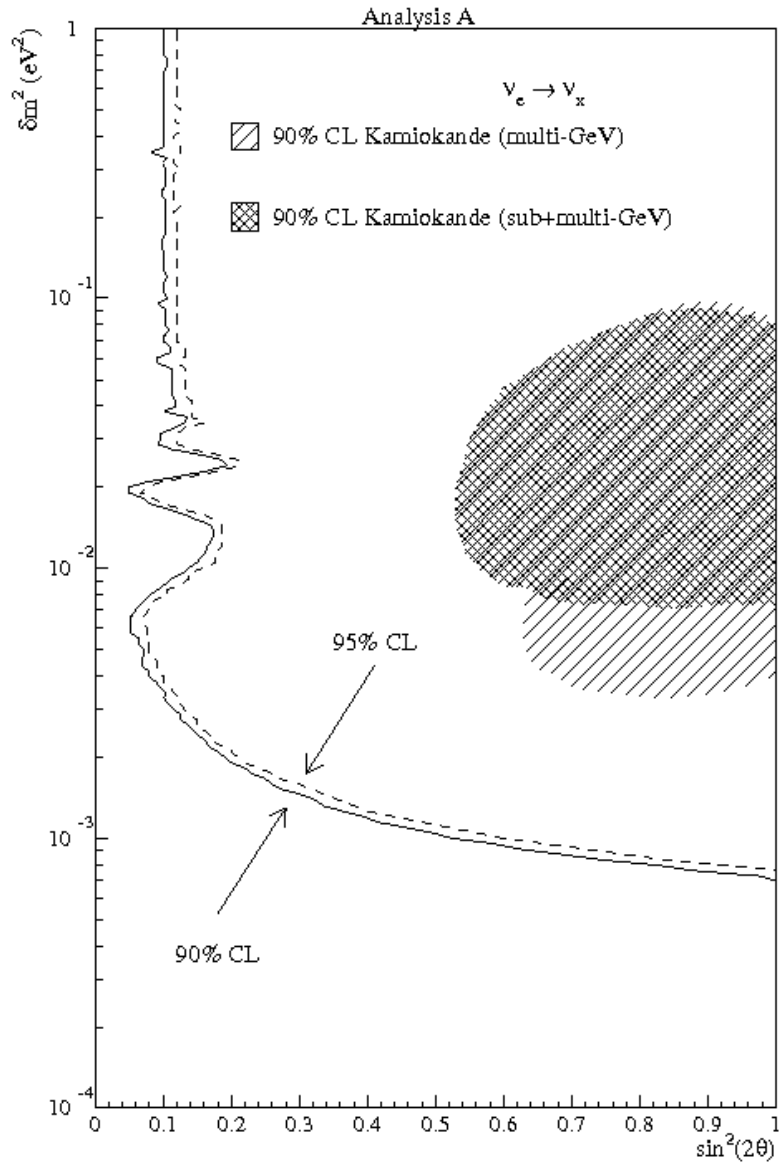

Figure 2.4: Exclusion plot of $\nu_e \leftrightarrow \nu_\mu$-oscillations. The CHOOZ experimental results exclude the $\nu_e \leftrightarrow \nu_\mu$-channel as a possible explanation for the atmospheric neutrino anomaly. The Kamiokande results are completely situated in the oscillaton area of Δm^2 and $\sin^2 2\theta$ that is excluded by the CHOOZ results.

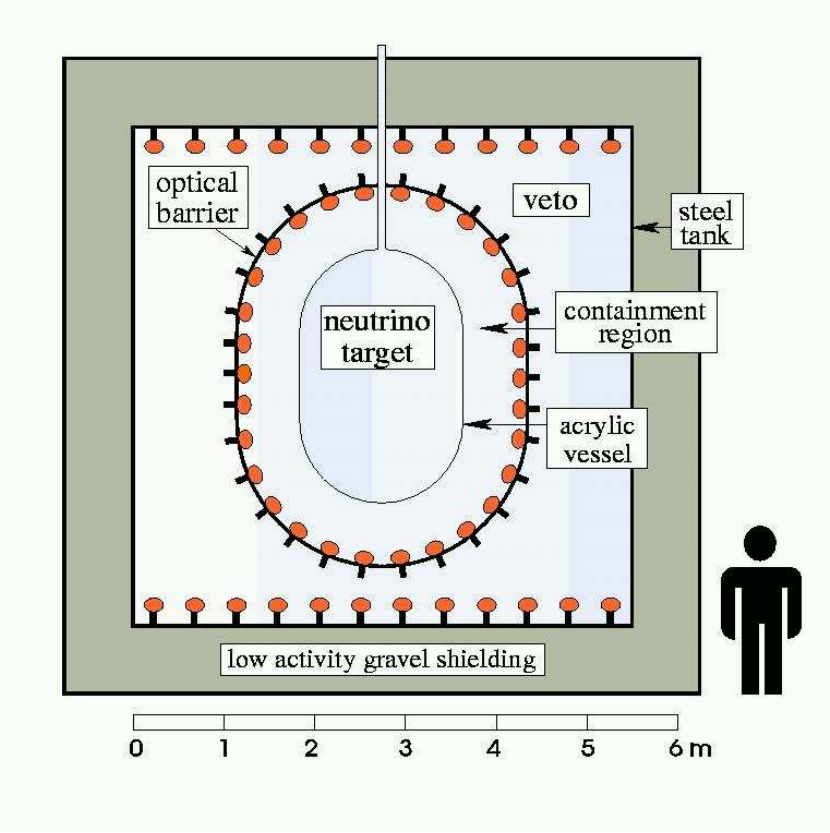

Figure 2.5: Schematic view of the CHOOZ-detector.

magnetic field and solar winds. Once in the atmosphere, the primary cosmic particles immediately interact with nuclei and thereby initiate a particle shower in the air. A cascade of secondary particles is created as shown in Figure 2.6. This inelastic interaction produces neutrons, pions, kaons, and other mesons of very short lifetime. The main production channel for muons is the decay of charged pions and kaons at a high atmospheric altitude ($\sim 15\,\mathrm{km}$).[26] Due to the relativistic effect of time dilatation, muons are able to reach sea level where they are the most abundant secondary particles.
Muons and neutrinos are the only cosmic rays that penetrate through matter to considerable depths of several hundred meters of water equivalent. Through hadronic and electromagnetic showers, muons can produce neutrons, photons, and electrons. The production of neutrons is discussed in

[26] At lower atmospheric levels, where the density is much higher, pions mainly decay through nuclear reactions.

Section 2.3.1. Two of the most important interaction mechanisms of muons in matter are:

- **Ionization**
  In matter, charged particles like muons ionize the atoms. The energy loss of the ionizing particle per distance is given by the Bethe-Bloch formula:

$$-\left(\frac{dE}{dx}\right)_{Ion} = \frac{4\pi}{m_e c^2}\cdot\frac{nz^2}{\beta^2}\cdot\left(\frac{e^2}{4\pi\epsilon_o}\right)^2\cdot\left[\ln\left(\frac{2m_e c^2\beta^2}{I\cdot(1-\beta^2)}\right)-\beta^2\right], \quad (2.25)$$

  with the following parameters: $\beta = v/c$, v = velocity of the particle, E = energy of the particle, x = distance travelled by the particle, c = speed of light, z = particle charge (in units of e), e = elementary charge, m_e = rest mass of the electron, n = electron density of the target, ϵ_0 = permittivity of free space, I = mean excitation potential of the target.

- **Bremsstrahlung**
  Through deflection in the Coulomb field of atoms, charged particles are decelerated. This deceleration is caused by a conversion of kinetic energy into electromagnetic radiation with continuous spectrum. In contrast to the ionization effect, the energy loss through Bremsstrahlung is proportional to the energy of the incoming particle and can be described as

$$-\left(\frac{dE}{dx}\right)_{Brems} = 4\alpha\cdot N_A\cdot\frac{Z^2}{A}\cdot z^2\left(\frac{1}{4\pi\epsilon_0}\cdot\frac{e^2}{mc^2}\right)^2\cdot E\ln\frac{183}{Z^{1/3}}, \quad (2.26)$$

  with E = energy of the particle, x = distance travelled by the particle, α = fine structure constant, N_A = Avogadro constant, Z = atomic number of the target, A = mass number of the target, z = particle charge (in units of e), ϵ_0 = permittivity of free space, e = elementary charge, m = mass of incoming particle, c = speed of light.

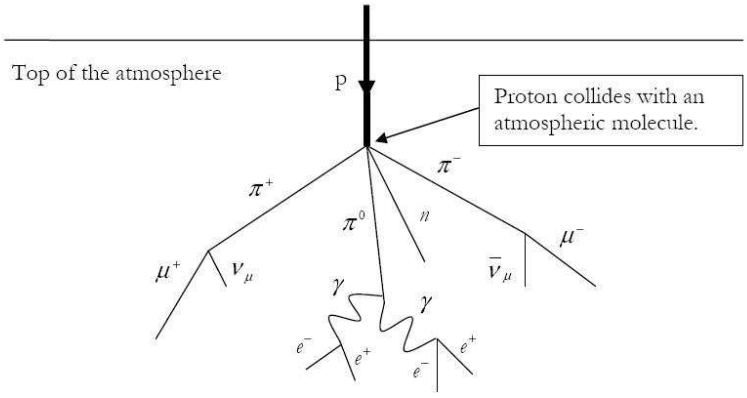

Figure 2.6: Schematic drawing of a proton induced particle shower in the atmosphere.

2.3.1 Production of neutrons

There are four main processes of neutron production from cosmic muons in matter [33]:

- A muon is captured by a nucleus followed by a neutron emission. This effect is more relevant for depths of less than 300 m.w.e. and will therefore be more important to the DoubleChooz near detector.

- The deep inelastic scattering of a muon with a nucleus is called *direct muon spallation*:

$$\mu + \text{Nucleus} \rightarrow \mu + \text{Nucleus}^* + n \tag{2.27}$$

- Indirect neutron production takes place when hadrons are generated in muon induced nuclear showers. While protons produced in the hadronic cascade rapidly lose their energy by ionization effects, neutrons in the cascade can even multiply further. The capture of a slow π^- by a nucleus is another way of producing neutrons.

- Another indirect production channel of neutrons is possible. It originates from photons coming from muon induced electromagentic showers. There are two possibilities with electromagnetic showers as a source of neutron generation. They both include photons. They are

$$\gamma + (Z, A) \rightarrow (Z - 1, A - 1) + n + \pi^+, \tag{2.28}$$

and as a 2-step reaction

$$\gamma+(Z,A) \rightarrow (Z,A)+\pi^+\pi^- \qquad \pi^-+(Z,A) \rightarrow (Z-1,A-1)+n. \quad (2.29)$$

In order to estimate the contribution of muon induced neutrons to the background, it is important to know the production rate of neutrons per muon N_n. It has been shown that this value depends on the average muon energy $\langle E_\mu \rangle$ at a certain depth h [34]:

$$N_n(h) \propto \langle E_\mu(h) \rangle^{0.75}. \quad (2.30)$$

A Monte Carlo simulation was performed in order to deliver a unified approach to experimental results from different depths. It yielded the equation

$$N_n = \frac{4.14}{\mathrm{g \cdot cm^{-2}}} \times \left(\frac{E_\mu}{\mathrm{GeV}} \right)^{0.74} \times 10^{-6} \times \rho \times h \quad (2.31)$$

for the number of neutrons produced per muon in dependence on the type of matter traversed by the muons. ρ and h are density and heigth of the corresponding material [35]. This is consitent with (2.30) and will be of concern in Section 5.2.2.

Chapter 3

The DoubleChooz Experiment

Situated in the Ardennes region in northern France, close to the Belgian border, the Chooz-B nuclear power station is one of the most powerful reactor plants in the world. The two pressurized water reactors produce an electrical power of 1.5 GW each [36] and went into service in 1997. They act as an antineutrino source for the DoubleChooz experiment which will be placed on the reactor site (see Figure 3.1). It is the successor of the Chooz experiment that was investigating θ_{13} with one single detector at the end of the 90's. If successful, the DoubleChooz results will provide a guideline for future long baseline experiments to search for CP-violation and further examine matter effects. The international DoubleChooz collaboration consists of universities and research institutions from Brasil, France, Germany, Italy, Japan, Russia, Spain, UK, and the USA.

3.1 Experimental Concept

Double Chooz is a reactor antineutrino dissappearance experiment that aims at finding the value of the third neutrino mixing angle θ_{13} by comparing neutrino flux and spectrum of two identical detectors at different distances to the reactor cores. Since matter effects and CP-violations[1] do not have to be taken into account and facilities and infrastructure of the former Chooz experiment can be used again, Double Chooz will offer a cost-effective discovery potential for the only still unknown neutrino mixing angle. The two

[1]The detection principle (inverse beta decay) is independent of parameter degeneracies induced by the CP-δ phase. Low $\bar{\nu}_e$ energies and short baselines avoid matter effects that could disturb the measurement [37].

Figure 3.1: The Chooz reactor plant with positions of DoubleChooz near and far detectors.

detectors will be placed at distances of 280 m and 1.05 km from the reactor cores. Except for different overburdens of rock serving as muon shielding, the detectors will be identical. Within phase 1 of the experiment, only the far-detector will start taking data. It will be built in the already existing underground laboratory of the Chooz experiment and go into service in the beginning of 2009. In phase 2 starting probably in early 2010, the near-detector will join the experiment and dramatically increase the sensitivity by one order of magnitude to $\sin^2 2\theta_{13} \approx 0.03$ (see Figure 3.2). The fact of having two identical detectors at different distances to the reactor cores allows to cancel out systematic errors coming from an imprecise knowledge of reactor properties which marks the major advantage of a two-detector experiment. The aim is to achieve an overall systematic uncertainty below 0.6% [38]. While the near detector will monitor absolute values as a reference, the far one is supposed to measure deviations from the expectations that suggest oscillation effects.
Besides this main area of application, the detector concept could also be of value for the United Nations (UN) and its International Atomic Energy Association (IAEA) for non-proliferation efforts.
Table 3.1 summarizes some important experiment parameters.

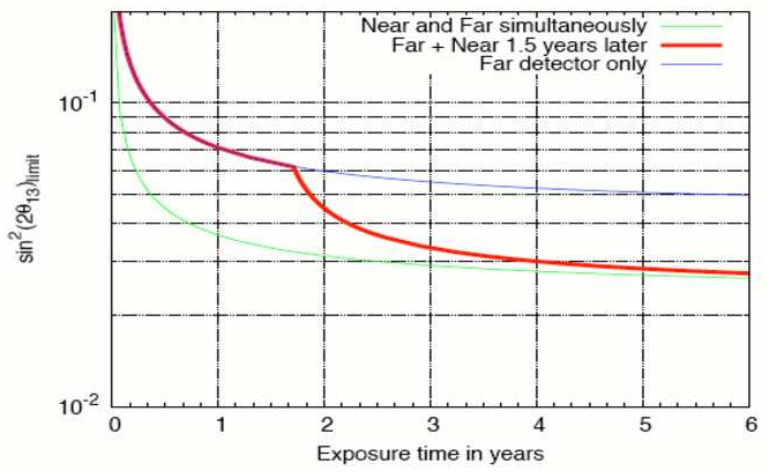

Figure 3.2: Expected sensitivity to measurement of $\sin^2 2\theta_{13}$

Reactor Thermal Power	2x 4.27 GW
Reactor Electric Power	2x 1.5 GW_e
Near Detector Distance	∼280 m
Far Detector Distance	1050 m
Near Detector overburden	70-80 m.w.e.
Far Detector overburden	300 m.w.e.
Running time Far Detector only (Phase 1)	1-1.5 a
Running time both Detectors (Phase 2)	3 a
Target volume	10.3 m^3

Table 3.1: DoubleChooz: Important parameters.

3.2 Scintillation based $\bar{\nu}$-Detection

3.2.1 Detection principle

By the use of two identical detectors at different distances to the neutrino source, systematic errors originating from a lack of knowledge of the antineutrino flux and spectrum from the the nuclear reactors can be minimized. The reference for the deviations measured by the far detector will be the data collected by the near detector. In this way, the oscillation signal can be determined independently from uncertainties and with greatly reduced systematic errors.
While there are in general three available detection interactions, the investigation of only one of them is reasonable [8]. The elastic scattering of a neutrino with an electron lacks a large enough cross section as well as a perceptible signature. Furthermore, neutrinos can interact via neutral current (involving the exchange of a Z boson) or charged current (involving the exchange of a W boson) weak interactions. In a neutral current interaction, the neutrino leaves the detector after having transferred some of its energy and momentum to a target particle. All three neutrino flavors can participate regardless of the neutrino energy. However, no neutrino flavor information is left behind. At DoubleChooz, this way to detect neutrinos does not work either because the comparably low $\bar{\nu}_e$-energies of up to about 12 MeV (see Figure 3.3) do not allow pion production and the remaining nuclear recoil of some keV is not detectable with the used technique.

In a charged current interaction, the neutrino transforms into its partner lepton. Since the interaction involves the exchange of a charged boson, the target particle also changes character. A charged current reaction of the incoming antineutrino and a proton in the target is used for detection at DoubleChooz. This reaction is called inverse β-decay (see Figure 3.4):

$$\bar{\nu}_e + p \rightarrow e^+ + n \tag{3.1}$$

This reaction is most suitable because it has the highest cross section for typical reactor antineutrino energies (eg. $\sim 5.7 \cdot 10^{-42}\,\mathrm{cm}^2$ for $E_\nu = 9\,\mathrm{MeV}$; see Figure 3.5) [27]. The resulting particles (positron and neutron) generate a very characteristic signal.
The positron immediately annihilates with an electron producing two monochro-

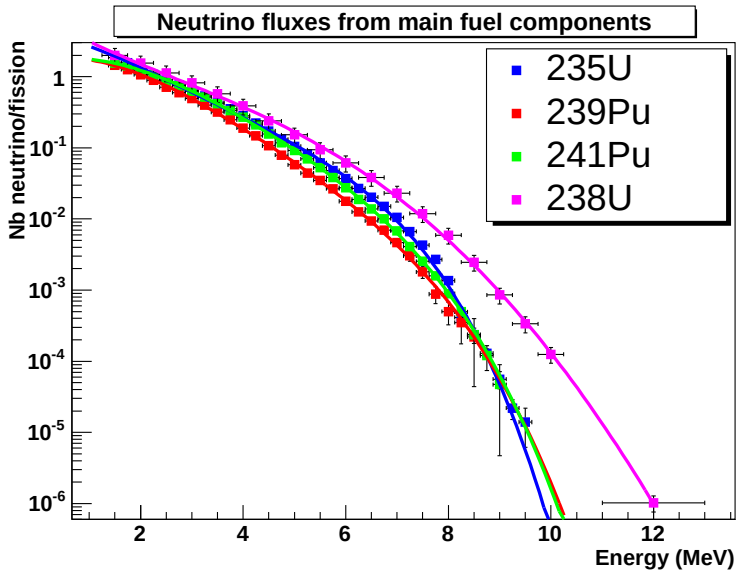

(a) Energy spectrum of reactor antineutrinos. No antineutrinos with $E_{\bar{\nu}_e} > 12\,\mathrm{MeV}$ are generated at the reactor cores.

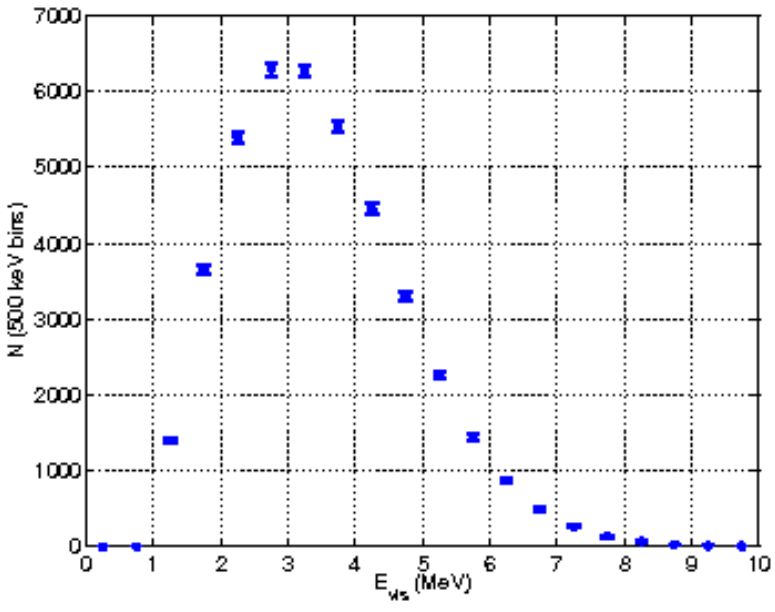

(b) Expected positron energy spectrum at the far detector for three years of data taking assuming true values of $\sin^2(2\theta_{13}) = 0.1$ and $\Delta m^2_{31} = 2.5 \times 10^{-3}\mathrm{eV}^2$

Figure 3.3: Reactor antineutrinos in the detector [36].

matic, back-to-back photons[2] with an energy of $E_\gamma = m_e = 0.511\,\mathrm{MeV}$ [4]:

$$e^+ + e^- \rightarrow \gamma\gamma \tag{3.2}$$

The thermal neutron, after decelerating over a distance of about 5 cm through impacts with nuclei, is captured either on hydrogen or gadolinium. The stimulated nucleus returns to the ground state via γ-emission.

$$n + Gd \rightarrow Gd^* \rightarrow Gd + \sum_i \gamma_i \tag{3.3}$$

In the case of Gd, the γ-cascade has an energy of 8 MeV with an average number of photons of $N_\gamma \simeq 3$. This γ-radiation is detected by the scintillator in target and γ-catcher as a delayed signal compared to the two gammas coming from the e^+e^--annihilation. Therefore, the distinct signature for the inverse β-decay (3.1) consists of two gamma-signals, clearly separated by a few μs. A time window in the magnitude of μs is used in the neutrino signal trigger as a specification that separates the typical character of two correlated events from accidental backgrounds. This procedure is called coincidence measurement.[3] This typical pair of signals allows a rejection of most of the background.

Using (3.1), the incoming antineutrino energy is

$$E_{\bar{\nu}_e} = \frac{1}{2}\frac{2M_pE_{e^+} + M_n^2 - M_p^2 - m_e^2}{M_p - E_{e^+} + \cos\theta\sqrt{E_{e^+}^2 - m_e^2}}. \tag{3.4}$$

The visible energy is the energy that can be observed with the detector. It is defined as the positron energy plus its annihilation on an electron. Together with (3.4) it is

$$E_{vis} = E_{e^+} + m_e \simeq E_{\bar{\nu}_e} - \Delta + m_e = E_{\bar{\nu}_e} - 0.782\,\mathrm{MeV}, \tag{3.5}$$

introducing $\Delta = M_n - M_p = 1.293\,\mathrm{MeV}$.

[2]During the rapid deceleration process of the positron, further photons emerge. They also contribute to the detection process.

[3]The time of $\sim 200\,\mu s$ for the thermal neutron to be captured is reduced to $\sim 30\,\mu s$ by doping the target scintillator with Gd. This reduction minimizes the number of possible background sources that could disturb the signal (see 3.2.2).

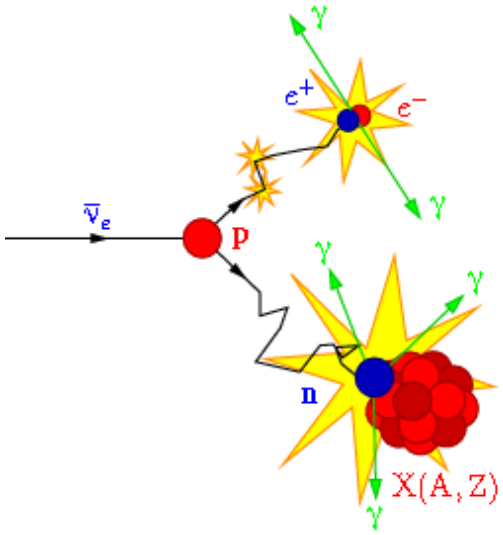

Figure 3.4: Schematic view of antineutrino reaction used for detection (inverse β-decay) [8]. The Figure is not to scale.

3.2.2 Expected backgrounds

The very small interaction cross sections of neutrinos demand a precise knowledge of the background in neutrino detection experiments. At DoubleChooz, the investigation of backgrounds is a crucial premise to find purity limits for the detector components and to estimate dimensions for the overburden of the near detector. Background signals in the detector originate from primordial and man-made radioactivity as well as from cosmic ray interactions. While the exclusive use of high purity materials and passive shielding helps to keep the radioactivity-related background under control, cosmic muons have to be dealt with carefully. γ-, β-, and n-interactions in the target area can create signals with a signature similar to e^+e^--annihilation whereas the Gadolinium in the target also captures neutrons that have origins other than the inverse β-decay. Besides these accidental background reactions, cosmic muons in the GeV range (eg. 63 GeV for the far detector, as shown in Figure 3.6) are also a source of correlated background events[4].

[4]A neutron like event, by chance releasing energy in the time window after a different event in the scintillator of above 1 MeV is called accidental. Here two random, uncorrelated events simulate the e^+n-signal of the inverse β-decay. The rate of accidental background events is proportional to the single event rates and the lenght of the time window: $R_{acc} \sim R_1 \cdot R_2 \cdot \tau$. Neutrons depositing energy in the scintillator through slowing down and then

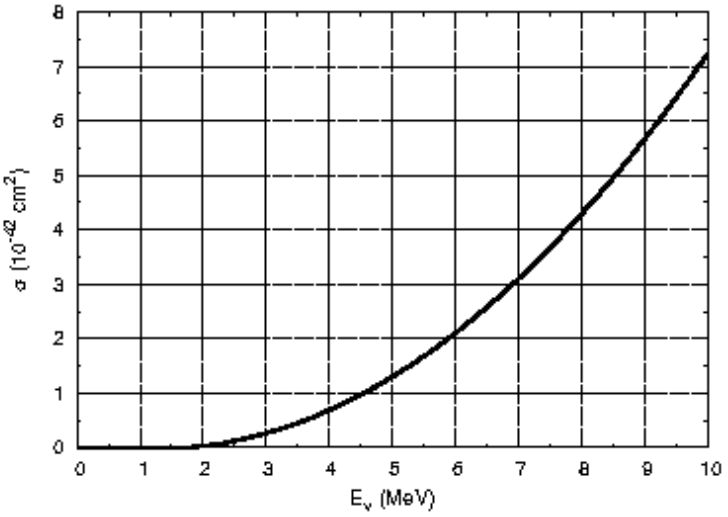

Figure 3.5: Cross section of $\bar{\nu}_e$-energies - A precise knowledge of the background is required [36].

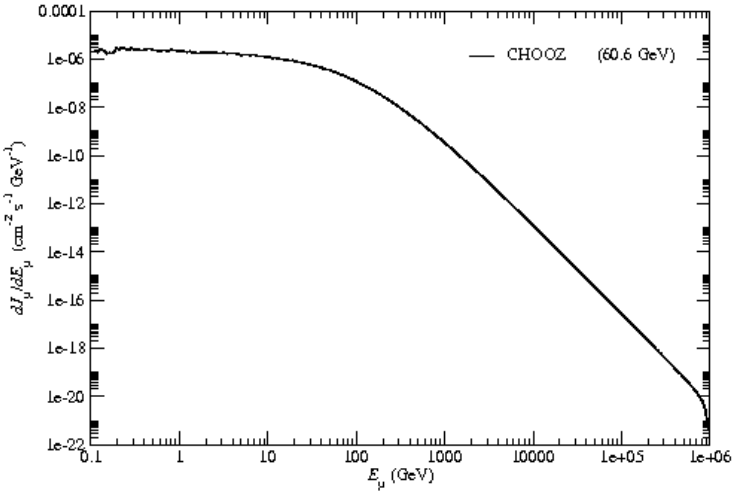

Figure 3.6: Cosmic muons at the far detector (energy spectrum) [36].

It is assumed that correlated background events are the biggest threat to the experiment [37]. Here, two kinds of correlated events deliver the main contribution to that background, β-neutron cascades and very fast external neutrons, both coming from spallation processes of high energy cosmic muons. The latter is studied in this work.

- **Beta-neutron cascades**
  In the scintillator, spallation processes of cosmic muons on ^{12}C may generate ^{9}Li, ^{11}Li, and ^{8}He. A β-decay of those elements that emits a neutron can then mimic a neutrino event (see Table 3.2). This kind of background is particularly dangerous for shallow depth experiments such as CHOOZ and DoubleChooz since muon rates are too high to allow a precise veto detection. Estimations lead to an expected background event rate caused by beta-neutron-cascades of $0.4 - 2\,\mathrm{d}^{-1}$ for the far detector.

- **Fast external neutrons**
  A spectrum of fast neutrons produced by near-miss muons[5] can generate an imitation of the delayed gamma-signal that is typical for antineutrino-events. When the fast neutrons decelerate through scattering, recoil protons are able to produce a detector signal of above 1 MeV. Combined with the following neutron capture on Gd, a neutrino event can be emulated. A rough estimation, taking into account former CHOOZ results, yields a rate of neutrons in the dangerous energy window ($2 - 8$ MeV) of approx. 1 event per day at 90 % C.L. (Confidence Level). In order to obtain this result, a simulation had been written with the purpose of reproducing the CHOOZ experimental results. It was aligned with the DoubleChooz geometry. In this way it was possible to study the effects of the different detector design on the neutron rate coming from CHOOZ [6] [39].

being captured on Gd cause correlated background. Here both parts of the signal (e^+ and n) are simulated by the same background event.

[5] As opposed to muons that directly hit the detector and are thus seen by the veto, near-miss muons remain invisible and can therefore become a threat to the experiment.

[6] The different materials chosen as a shielding (sand in CHOOZ vs. steel in DoubleChooz) result in a smaller mean free path for neutrons in DoubleChooz. On the other hand the bigger target at DoubleChooz yields a larger area of exposure to fast neutrons.

	Branching Ratio	Decay Mode	Resulting Element
^{8}He	88 %	$\beta^- < 9.6\,\mathrm{MeV}$	^{8}Li
	12 %	$n + \beta^- < 8.6\,\mathrm{MeV}$	$^7\mathrm{Li} + n$
^{9}Li	51 %	$\beta^- < 13.6\,\mathrm{MeV}$	^{9}Be
	49 %	$n + \beta^- < 11.9\,\mathrm{MeV}$	$^8\mathrm{Be} + n$

Table 3.2: Branching ratios for the decay of ^{8}He and ^{9}Li isotopes. Neutrons emitted in these decays are typically around 1 MeV.

Detector	Rock overburden (m.w.e.)	BR [1/d]	DR [1/d]
near	60	9-23	1012
far	300	0-5	69

Table 3.3: Expected total background rates (BR) and antineutrino detection rates (DR) for Double Chooz detectors.

Considering the low expected antineutrino detection rates in the detectors, the importance of an effective background reduction and understanding becomes clear (see Table 3.3). A signal to noise ratio of 100 is desired. Together with the systematic error, the background defines the sensitivity to $\sin^2(2\theta_{13})$ and is therefore crucial to the success of the experiment.

3.2.3 Systematic errors

The total systematic error of the Chooz experiment was 2.7 %. For Double-Chooz, the aim is to reduce this error to 0.6 %. The two detector concept cancels out the necessity to deal with the 2 % uncertainty in the knowledge of the reactor antineutrino flux which was the main error contribution at

	CHOOZ	DoubleChooz
Reactor cross section	1.9 %	-
Number of protons	0.8 %	0.2 %
Detector efficiency	1.5 %	0.5 %
Reactor power	0.7 %	-
Energy per fission	0.6 %	-
TOTAL	∼2.7 %	∼0.6 %

Table 3.4: Composition of systematic errors for CHOOZ and DoubleChooz.

CHOOZ (reactor cross section, reactor power and energy per fission can be seen in Table 3.4) [40]. The DoubleChooz near detector will monitor the reactor antineutrino flux. Furthermore, an improved detector design, respecting the gained insights from CHOOZ, will help to minimize the error. For instance, a steel shielding will be used instead of the sand applied at CHOOZ and a non-scintillating buffer region will further reduce the single rate in the target region by decreasing radioactive effects coming from impurities of the photomultiplier tubes. The biggest error sources of DoubleChooz lie in the calibration and normalization between the two detectors (number of protons in the target vessels and detector efficiencies in Table 3.4). Some of the most important factors are listed below. An overview of their contribution to the total normalization error is given in Table 3.5.

- **Solid angle**
  The distances between the detector centers and the reactor cores have to be precisely known. A measurement accuracy of 10 cm was achieved by the CHOOZ experiment. This absolute value becomes more effective for DoubleChooz as the total distance for the near detector will be only 250-300 m.

- **Hydrogen nuclei**
  The number of hydrogen atoms in the detector liquids is very difficult to measure. A forecasted uncertainty of about 1 % can be further reduced by preparing the liquid for both detectors in one load. This won't improve the total error, but guarantees the same quantity of H nuclei in near and far detector.

- **Dead time**
  The different rock overburdens at near and far site result in different cosmic muon rates reaching the veto areas. The rate will be of a factor 30 higher for the near detector. The constant dead time that is applied to each through going muon will thus add up to very different total dead times of the detectors.

- **Particle identifications**
  The typical antineutrino detection process through inverse β-decay includes some sources for systematic errors. One of the 511 keV gammas generated in the prompt e^+e^--annihilation may leave the target region. Due to the fact that it will still deposit most of its energy in the target

			CHOOZ	DC
Reactor		Solid Angle	-	0.06%
Detector	H nuclei	Volume	0.3%	0.2%
	in target	Fiducial Volume	0.2%	0
		Density		0.1%
		H/C	0.8%	0
Detector	Electronics	Dead Time	-	0%
Particle	Positron	Escape	0.1%	0
Identification		Capture	0	0
		Energy Cut	0.8%	0.2%
Particle	Neutron	Escape	1.0%	0
Identification		Capture (% Gd)	0.85%	0.3%
		Identification Cut	0.4%	0.1%
Particle	Antineutrino	Time Cut	0.4%	0.1%
Identification		Distance Cut	0.3%	0
		Unicity	0.5%	0
Total			1.5%	0.5%

Table 3.5: Total systematic normalization errors and detector efficiency between the detectors - CHOOZ vs. DoubleChooz.

area and that energy cuts will exclude almost none of the positrons, the systematic error can be neglected. For the delayed neutron signal, the absolute gamma-spectrum from the capture on Gd or H may not be known precisely. Still, the applied energy selection cut will contribute to the systematic error. Also the time for a neutron capture on Gd is not known exactly. Compared to CHOOZ, the DoubleChooz concept offers the possibility to do a relative comparison between the two detectors which reduces the associated systematic error to the control on electronic time cuts.

3.3 Detector Components

From the center to the inner muon veto, the two cylindrical detectors will be identical. The detectors will have a size and a diameter of 7 m. In order to compensate differences in intensity of the cosmic background due to the

different rock overburdens[7] of the far and near laboratory, outer shielding and outer muon veto will be of different dimensions. Beginning from the inside, the different detector elements are as follows (see Figure 3.7):

- **Target**
  The target is the main part of the detectors. Here the $\bar{\nu}_e$-interactions are observed. 10.3 m^3 of liquid scintillator doped with 0.1% of Gadolinium [41] will be inside an acrylic cylinder of 115 cm radius and 246 cm height. The acrylic vessel will be fully transparent to γ-radiation with a wavelength of $\lambda > 400$ nm.

- **γ-Catcher**
  A 55 cm thick buffer region of undoped liquid scintillator with a total volume of 23.6 m^3 is built around the target. The γ-catcher will be used together with the target as a calorimeter to measure energy-spectra with two main purposes. On the one hand, the possibility to consider gammas from antineutrino interactions that happen close to the frame of the target is provided. The energies can range from 0.5 MeV for gammas from e^+e^--annihilation to ~8 MeV for gammas originating from neutron-capture on Gadolinium[8]. On the other hand, the gamma-catcher is necessary to efficiently reject specific background that is created by fast neutrons originating from muons crossing the rock near the detector (cp. section 2.3). Results of previously executed simulations agree with the chosen width of 55 cm as the optimum size for the gamma-catcher.

- **Buffer**
  Around the target region, a 105 cm thick stainless steel vessel is filled with 104.2 m^3 of non-scintillating mineral oil. This buffer prevents target and gamma-catcher from accidental backgrounds such as radioactivity coming from photomultiplier tubes (PMT's) and other construction materials. An accidental rate below 10 Hz will be achieved. About 400 PMT's are mounted on the outer buffer wall and measure gamma radiation from the scintillation processes inside the target area.

[7] 300 m.w.e. for the far lab compared to ~70-80 m.w.e. for the near lab, depending on the final decision on location, drill depth etc.

[8] The mean number of γ's released from neutron capture is 3-4, but in the case of a single gamma, energies up to 8 MeV are possible

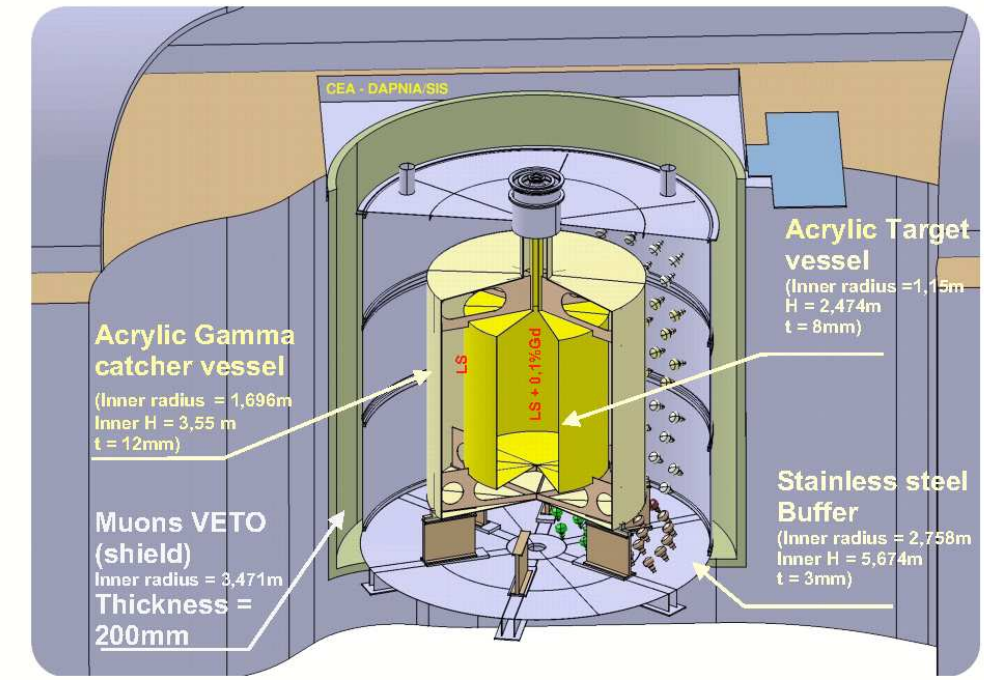

Figure 3.7: The different layers of the DoubleChooz detector.

- **Inner Veto**
  A volume of liquid scintillator with a thickness of 50 cm around the buffer region and 78 photomultipliers on the outer wall detects cosmic muons as well as cosmic muon induced backgrounds and marks associated events. Additionaly, a shielding of 15 cm thick steel further reduces external gamma backgrounds [42].

- **Outer Veto**
  Many square layers of plastic scintillator with a size of 49 m^2 above the detectors are read out by dedicated photomultipliers. The outer veto further decreases the muonic background. Its thickness differs considerably between near and far detector as for the near detector it has to compensate the much lower rock overburden due to the shallower depth of the laboratory.

Chapter 4

Simulation and Software Tools

The following chapter presents the software environment that was used for the simulations and analyses in this work. In the development phase of particle physics experiments, software simulations can help to improve the accuracy of the experiment by contributing to research and development of the detector design. Concerning the muon veto for instance, simulations can provide answers to the questions of PMT placement and classification of muon and neutron rates. Also the practicability of the project in general can be ensured using simulations. Therefore, a simulation software must comprise the complete physical spectrum of detector properties, particle transport, background behaviour and electronic effects [36]. In order to guarantee correctness of the simulation results, a strong implementation of existing data from prior experimental measurements is required. At this, the Double Chooz experiment has the advantage of being able to use experimental data from the similar Chooz experiment, that already partially used the infrastructure with comparable technics, as a reference for simulation works.
Later on, software tools accompany the experiment throughout the running phase as an important equipment for data analysis and physics discoveries.
The following sections will explain the main functions of the most important software tools used for simulations and data analysis.

4.1 The DOGS Environment

The **D**ouble Chooz **O**ffline **G**roup **S**oftware is the complete set of software packages that are specific to the Double Chooz experiment. It offers a com-

mon interface for communication and data exchange between the packages and can be installed as a whole. The two required external dependencies are Geant4 and Root (see Section 4.2) [43]. The packages and their functions are listed in Table 4.1. Two of those packages are now described more accurately.

4.1.1 Main simulation package DCGLG4sim

The **D**ouble **C**hooz **G**eneric **L**iquid Scintillator **G**eant**4** **sim**ulation is a special adaption of the GLG4sim Monte Carlo simulation software for the parameters and needs of Double Chooz. GLG4sim originates from a Geant4 based software written for the Kamland experiment 1999 in Japan and has become a generic library and starting point for specific liquid scintillator antineutrino detectors [44]. DCGLG4sim includes the detector geometry and marks the main feature of the DOGS environment. It propagates primary particles through the detector components and its surroundings and calculates the whole interaction process until the creation of photoelectrons in each PMT in order to find out the corresponding energy deposition in target and buffer regions. The Execution of DCGLG4sim works macro-based.[1] The software can be addressed by simple text files containing commands and specifications for the job to be taken. An example is given in Figure 4.1.

4.1.2 Electronics readout simulation DCRoSS

The **D**ouble **C**hooz **R**ead**o**ut **S**ystem **S**imulation package simulates the response of the detector readout system. Taking the DCGLG4sim Monte Carlo data as input, the detected photoelectrons will be converted to a digitized electrical signal that is now comparable to real experimental results since it takes into account the whole analogue to digital conversion process including the factors electronics, fluctuations, trigger logic etc. Considering the benefit of a simplified implementation as well as a prevention of difficulties in testing, empirical responses curves from test-benches are preferred to simulations behind the readout system in the architecture of DCRoSS.

[1] This also applies to DCRoSS and DCAna.

```
### deactivate hadronic processes
/glg4debug/glg4param omit_hadronic_processes  1.0

### rock shell around detector, source for fast neutrons
/glg4debug/glg4param rock_shell_thickness 5000.

### Store information about particles
/output/store/particles 1

### Time per event in ns
/generator/event_window 1e3

### initialize geometry
/run/initialize

### deactivates Cerenkov light
/process/inactivate Cerenkov

### deactivates scintillation
/glg4scint/off

### *** Simple test gun ***
### the next line specifies particle, start position (x,y,z), start
### momentum (x,y,z) and
### (optionally) start energy in MeV. If energy is given, momentum is
### treated as direction only
/generator/gun mu- 3260 0 4000 0 0 -1 63000

### Output file path and label
/event/output_file muon_EDep1

### Number of Events
/run/beamOn 1000
```

Figure 4.1: This facilitated excerpt from an input macro for DCGLG4sim displays some basic features of a cosmic muon simulation. The excerpt is taken from a simulation of $1000\,\mu^-$ with predefined momentum running through the steel shielding at the outer detector wall. For a complete simulation more commands are necessary. Short descriptions are above each command line.

Package	Description
DC Ana	Generic analysis code in the DOGS framework providing access to Root trees and event loops
DC Calib	Simulation of Calibration that is called up by DCReco and DCRoSS Implementation of decalibration effects into the DCRoSS package (eg. effects of defective PMT's)
DC Event	Passive package with the purpose of defining the complete data structure of the output files as well as establishing communication between different data structures of the DOGS packages
DC Geo	Administration of PMT positions from data files for DCReco, DCRoSS and DCGLG4sim
DC Reco	Reconstruction algorithms for inferring time and charge information and spatial reconstruction
DC Base	Support package providing functions that are needed by other packages (plotter, message system...)
DCGLG4sim	Monte Carlo based simulation for Double Chooz detectors (see Section 4.1.1)
DC NuGen	Stand alone code providing ν-interactions in the detector independently from simulation The resulting n and e^+ of the inverse β-decays are generated and can be used as direct input for DCGLG4sim
DC RoSS	Readout system simulation (see Section 4.1.2)

Table 4.1: Components of the DOGS package.

4.2 Other Software

Besides the DOGS package that is specific to the Double Chooz experiment, some other tools are applied in the simulation work.

4.2.1 Particle transportation framework Geant4

Geant4 (**Ge**ometry **an**d **t**racking) is a very well known platform for Monte Carlo based simulation of particles travelling through matter and is being developed at CERN. Besides geometry and tracking, it also deals with detector response, run management, and visualisation [45]. The Geant4 toolkit serves as substructure for the GLG4sim simulation program.

4.2.2 Analysis and visualisation library Root

The software package Root has also been developed at CERN. It is the main tool for analysis of Double Chooz simulation data as both DCGLG4sim and DCRoSS can store their outputs as tree objects in *.root* format. The functionality of Root covers histograms, graphs, statistics, and analysis of raw data [46].

4.2.3 Muon spectrum generation MUSIC

While muon rates can be measured quite reliably, the examination of muon energy spectra sometimes demands complex simulations [47]. The three dimensional Monte Carlo code MUSIC (**MU**on **SI**mulation **C**ode) describes muon propagation through rock. Most recent and accurate cross sections for interactions between muons and rock are implemented and angular deviation as well as lateral displacement due to effects like pair production and scattering are fully taken into account [48]. In the Double Chooz simulation environment, MUSIC is used to generate energy and angular distributions of cosmic muon radiation that the detector and the surrounding rock massive are exposed to.

Chapter 5

Studies of Muon induced Background

The following chapter focusses on the analysis of muon-induced background and its effects on future detector results. In this regard, near-miss muons[1] generating secondary particles such as photons and neutrons with the ability of reaching the detector target area are of special interest. These secondary particles have a potential of emulating the neutrino signal and thus need to be understood as precisely as possible. The major goal is to predict a rate and an energy spectrum of the muon-induced fast neutron background in the target area of the Double Chooz detectors.
After some examinations about the detector response to muonic background in terms of energy deposition and azimutal variation of muon input, the particlewise composition of the deposited energy is studied more accurately. Finally, a statement is made about muon-induced neutrons in the target area forming a potential hazard to unambiguous neutrino detection.

5.1 Basic Detector Response

In the following section, the exposure of the far detector to cosmic muons is simulated. Therefore, a set of muons with a fixed energy[2] is vertically injected into the circular steel shielding between inner muon veto and the

[1] Muons travelling through the steel shielding or the rock very close to the inner muon veto without being directly recognized.

[2] Corresponding to the expected average energy of cosmic muons reaching the far detector through the rock overburden.

Simulated particles	μ^-
Particle energy	63 GeV
Number of particles per simulation	1000
Dimension of steel shielding	3250 mm - 3410 mm
Approaching direction	Vertical
Min. particle tracklength	1 mm

Table 5.1: Simulation parameters for basic cosmic muon studies (Section 5.1). The dimension of the steel shielding refers to radial distances to the center of the concentric detector architecture. The minimum particle tracklength is a particle production cut in Geant4. Particles with an energy that only allows a mean free path of below 1 mm in the examined material are not produced. Their energy is directly deposited.

rock at different radial distances and angles relative to the detector center (see Figure 5.1). The energy depositions in target and inner veto and the resulting numbers of detectable photo electrons are examined with respect to the applied energy windows for neutrino detection of 1-10 MeV for the prompt signal and 2-8 MeV for the delayed signal. Table 5.1 summarizes some simulation parameters.

5.1.1 Dependence on radial distances of muon input

In this experimental series, simulations were done as listed in Table 5.1. The only variable parameter was the radial distance of the incoming muons towards the center of the detector within the steel shielding. 8 runs were done in steps of 20 mm from $r = 3260$ mm to $r = 3400$ mm. The mean values of the resulting 8 energy spectra for the different muon distances (see example in Figure 5.2) were extracted in order to investigate the dependence of the average energy deposition in the different detector areas on the location of muon injection.

Figure 5.3 shows the expected result of an exponential decrease of deposited energy with increasing radial distance. In this first approach, the sum of energy depositions of all involved secondary particles that were generated by the incoming muons like neutrons, electrons, and photons is used. This makes a precise explanation of the observed behaviour, taking into account effects of the different involved particle species, impossible at this point.

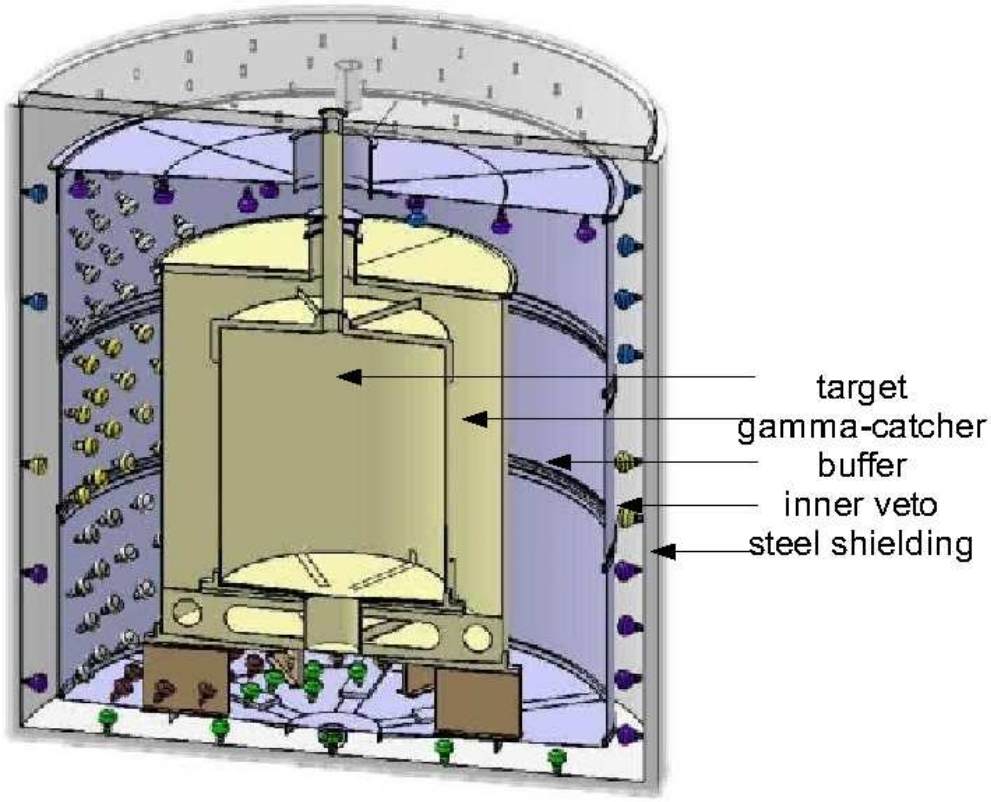

Figure 5.1: Layout of the Double Chooz detectors: Besides 87 PMT's on each of the bottom and the top caps, there are 30 equidistant vertical rows of PMT's on the cylindrical surface of the buffer. Hence, the angle between two vertical rows of photomultipliers is 12°. The layout of the veto PMT's with angles of 30° is only rudimentally indicated. The different detector elements are labelled.

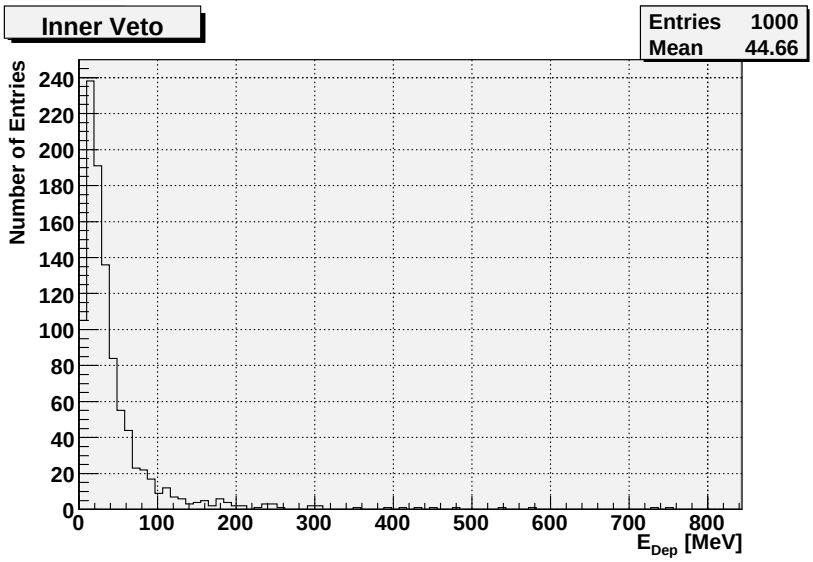

Figure 5.2: Example histogram for energy deposition (r=3300 mm). For the determination of radial dependences of the deposited energies, mean values are used instead of the complete distributions. This reduces the complexity of the task.

In Section 5.2, the involved secondary particles will be examined separately. Here, the *Absorption Law*

$$N(d) = N(0)e^{-\alpha d}, \tag{5.1}$$

with d being the penetration depth and α being the absorption coefficient (dependent on material and particle energy) gives a qualitative understanding of the exponential decrease of the deposited energy with an increase of steel depth which the secondary particles have to pass before reaching the detector.

In contrast to the simulation framework, the values of the energy deposited by the different secondary particles in the detector layers are not directly accessible in the experiment. Here, the visible parameter is the amount of photoelectrons produced by the photomultipliers after the scintillation process. This fact clarifies the necessity of precisely knowing how to regain information about the energy deposition from the measured signals. The detector architecture was particularly designed to provide a linear relation between the deposited energy and the number of measured photoelectrons resulting from that.

Figure 5.4 shows the number of photoelectrons in relation to r with a

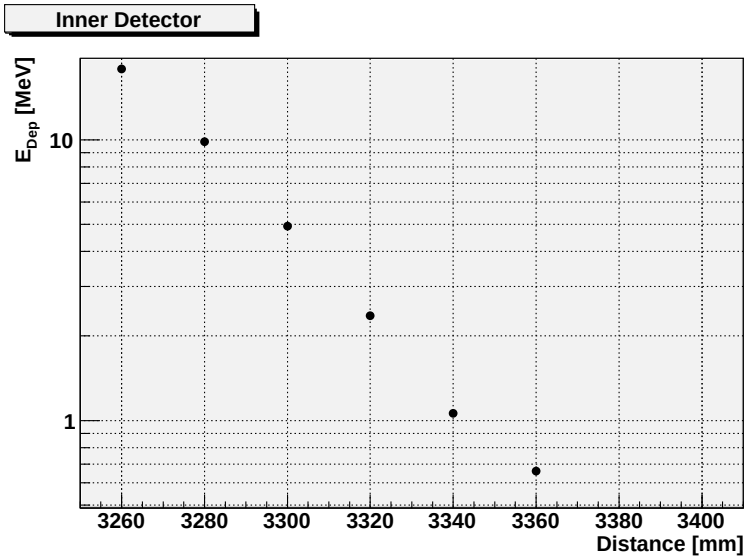

(a) Inner Detector (target+γ-catcher+buffer)

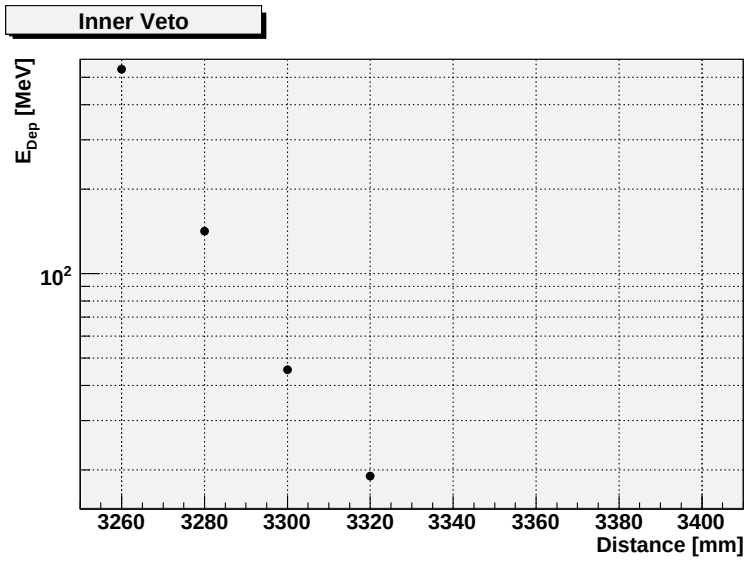

(b) Inner μ-veto

Figure 5.3: Mean Energy deposition over radial distance of muon injection from detector center for inner detector and inner veto.

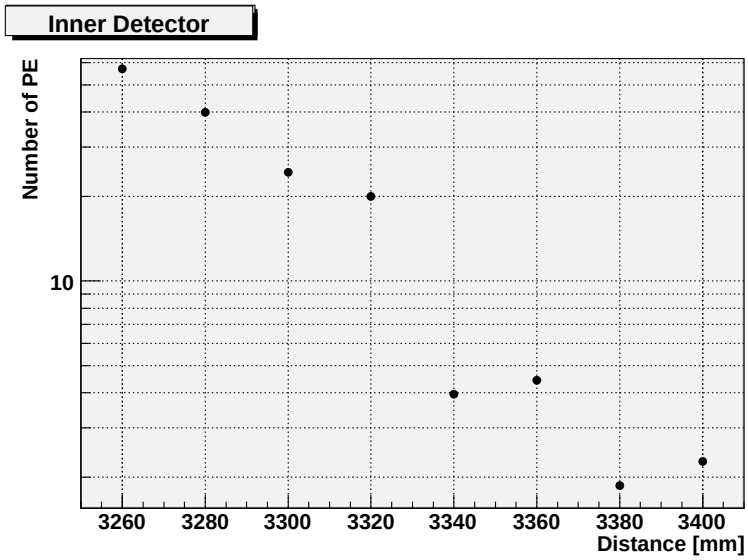

(a) Inner Detector (target+γ-catcher+buffer)

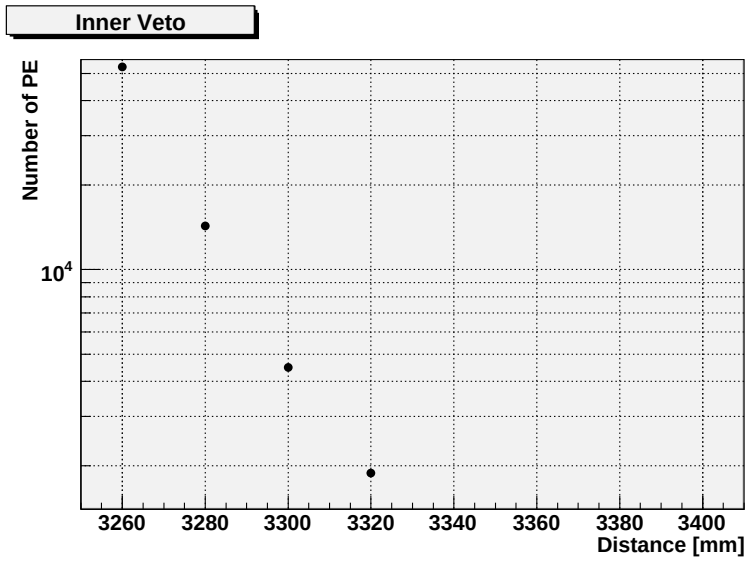

(b) Inner μ-veto

Figure 5.4: Number of photoelectrons over distance of muon injection.

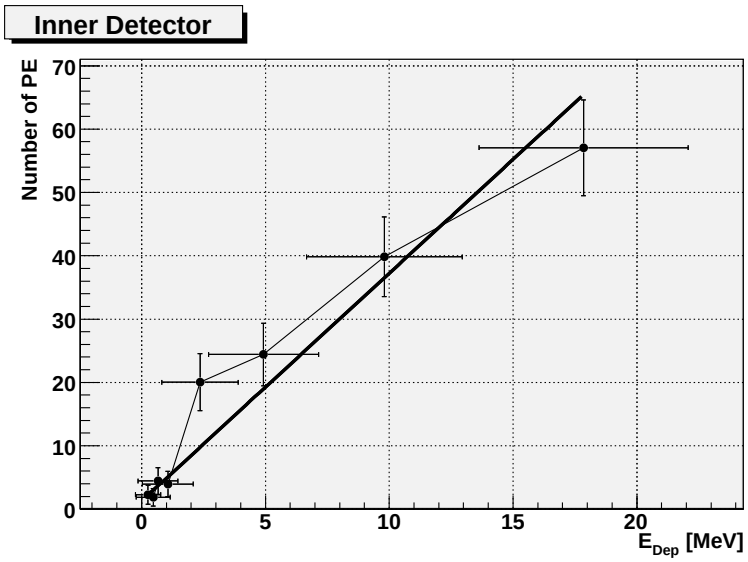

(a) Inner Detector (target+γ-catcher+buffer): $p0 = 1.28 \pm 0.88$; $p1 = 3.60 \pm 0.35$

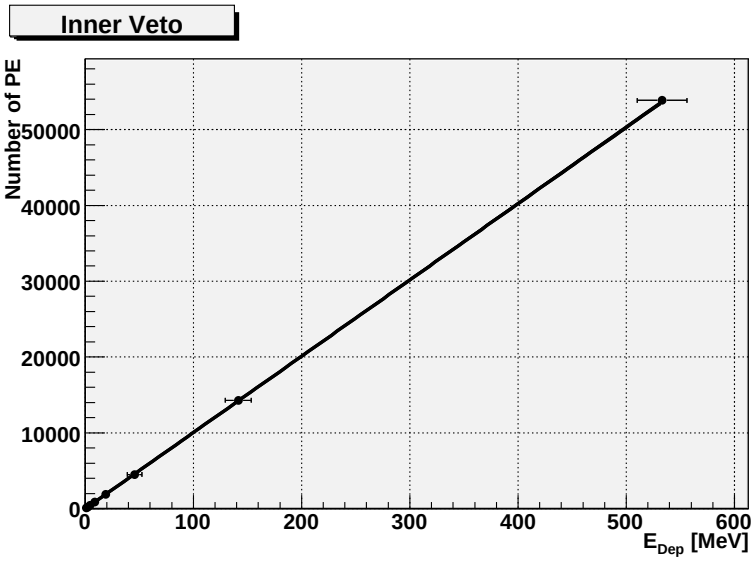

(b) Inner μ-veto:$p0 = -11.01 \pm 7.56$; $p1 = 100.59 \pm 0.37$

Figure 5.5: Number of photoelectrons over mean energy deposition at corresponding radial distances of muon injection with statistical errors. In both plots, a linear fit is used of which p0 is the y-axis intercept and p1 is the gradient. The connection lines in (a) are inserted for better visualisation only.

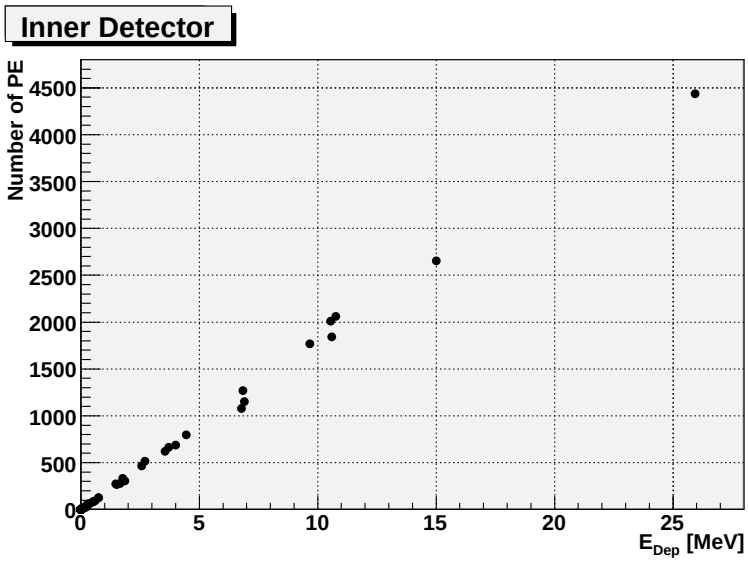

Figure 5.6: Number of photoelectrons over energy deposition for $r = 3300\,\text{mm}$ for target and γ-catcher only.

shape very similar to that concerning the energy deposition. The low statistics in the inner detector area explains deviations from exponential behaviour. The assumption of a linear relation between E_{Dep} and number of photoelectrons is confirmed for the veto by Figure 5.5 where those two parameters are directly compared. For the inner detector, one point does not fit to the assumption of linear behaviour within the error bars. This is to be traced back to the much lower statistics again. Taking into account the statistical errors for the linear fit, the graph in Figure 5.5(b) can be extrapolated to higher values.[3] A typical muon deposits $\sim$2 MeV/cm in the Veto region [49]. A muon vertically passing the whole veto with a height of 7 m results in a total energy deposition of $\sim$1400 MeV as a reference value for an energy deposition. Thus, an extrapolation to 1400 MeV produces 140815$\pm$10584 photoelectrons. Not only the amount of light produced by the passing muon can be a challenge to the photomultipliers (specially the ones close to the particle track), but also the electronic parts have to cope with the current that results as an answer from the PMTs to the detected amount of photoelectrons.
Figure 5.5(a) does not match with the expected amount of $\sim 180\,\text{PE/MeV}$ for the scintillator in the target region that is given in [27]. The buffer region

[3]The inner detector in Figure 5.5(a) is not designed for the detection of cosmic muons.

is included in the plot. Energy depositions in the non-scintillating buffer do not result in the production of photoelectrons. Figure 5.6 shows the production of photoelectrons per MeV for the scintillating areas of target and γ-catcher without the buffer at the muon injection distance $r = 3300\,\mathrm{mm}$. A linear fit to the plot results in a value of $178.2 \pm 2.5\,\mathrm{PE/MeV}$ which is in good accordance with the expected value. This result is a good cross-check of the functionality of the DOGS simulation software.

5.1.2 Effects of azimutal variation of muon input

In the following section, effects of the PMT positionings in inner veto and inner detector on the detection efficiency of energy depositions are studied for the first time.
In order to reach the required level of sensitivity, a high coverage of inner detector and inner veto with photomultiplier tubes is necessary. On the other hand, one has to deal with the downside, their radioactive impurities being the major source of uncorrelated internal background. With the experience gained at the CHOOZ experiment [27] (and also at Borexino and KamLAND), a photocathode coverage of $\sim$ 13.5% comes out as the best compromise. As described in Figure 5.1, for the inner detector region there is a distinct pattern of photomultiplier positioning in vertical rows each 12°. The PMT equipment of the inner veto region is done in the same scheme, but with a lower total amount of PMT's leading to a larger angle of 30° between adjoining tubes.
The PMT positions in the detector are now retraced with further simulations.[4] As opposed to Section 5.1.1, the simulation with the parameters of Table 5.1 is now done with a fixed radius at r=3300 mm. 24 muon injection points in steps of 15° build one loop around the circular steel shielding to examine effects of PMT placement on the amount of produced photoelectrons. The outcomes are displayed in Figure 5.7.
The number of photoelectrons rises with the proximity of the muon track to one coloumn of PMT's and reaches a local minimum for muons simulated in the steel at an angle in between two neighbouring coloumns. A lower distance between primary muons and photocathode means a lower amount of undetected scintillation light from energy depositions of secondary particles. This

[4]The simulations include positions of PMT's and light concentrators. Cables and mountings are not incorporated.

behaviour is verified for the inner veto in Figure 5.7(b) where the relation of the angle between PMT's of 30° and the simulation steps of 15° produces a periodical graph with deviations of up to $\sim 15\,\%$. The higher density of PMT rows in the inner detector of 12° prohibits the outcome of such a pattern for the same injection angles. Furthermore, statistical errors play a much bigger role due to the energy absorption of the muon veto in between muon input and buffer PMT's having a lower total amount of photoelectrons in the inner detector as a consequence. Still a clear variation of the generated number of photoelectrons can be observed underlining that effects of PMT alignment should not be neglected.

5.2 Composition of Detector Backgrounds

After the examination of global aspects like the total energy deposition in the detector in the previous section, the question of how different kinds of particles behave in the detector is now emphasized. Moreover, their contribution to the total amount of deposited energy is investigated. In this context, neutrons, electrons, and photons are studied more closely for the first time. Conclusions can be drawn about effectiveness of background rejection and correctness of size aspects of the detector architecture.
The cosmic muon simulations from Section 5.1 include the storage of secondary particles generated which are now studied more precisely at the 4 injection points $r_1 = 3280\,\text{mm}$, $r_2 = 3320\,\text{mm}$, $r_3 = 3360\,\text{mm}$, and $r_4 = 3400\,\text{mm}$. As Figure 5.8 shows, photons and electrons are the most abundant particles. Below $\sim$200 GeV cosmic muons in matter lose their energy mainly through ionization [49]. This explains the high production of electrons. Positrons and photons are then created along the way by electromagnetic showers. The thickness of the steel shielding is one crucial factor for an effective rejection of the electromagnetic background. Neutrons on the other hand, indeed being potentially most dangerous to the neutrino signal in the target area, are only produced at a very low rate.[5] In the executed simulation, only one neutron was generated. Hence, in order to make a statement about the detector reaction on fast neutron background, much higher statistics are required. For the purpose of obtaining a measurable neutronic

[5]The generated stable isotope of nitrogen N15 has, due to its higher cross section and recoil energy in steel, no chance of leaving the shielding and can therefore be neglected.

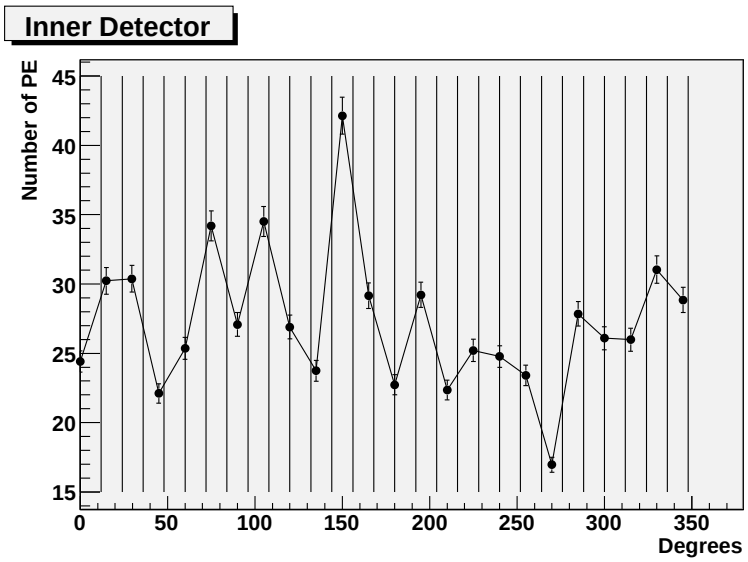

(a) Inner Detector (target+γ-catcher+buffer)

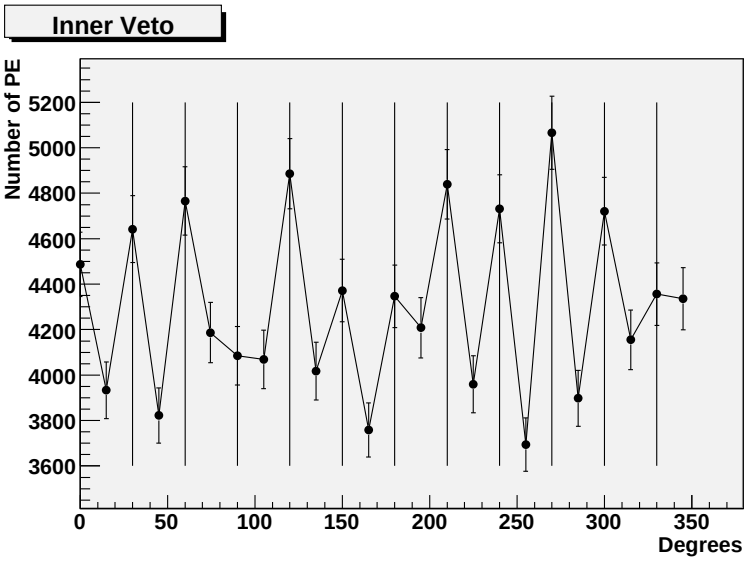

(b) Inner μ-veto

Figure 5.7: Number of photoelectrons over angular distribution of muon injection with statistical errors. The vertical lines indicate the positions of the vertical PMT rows. Connection lines are inserted for better visualisation only.

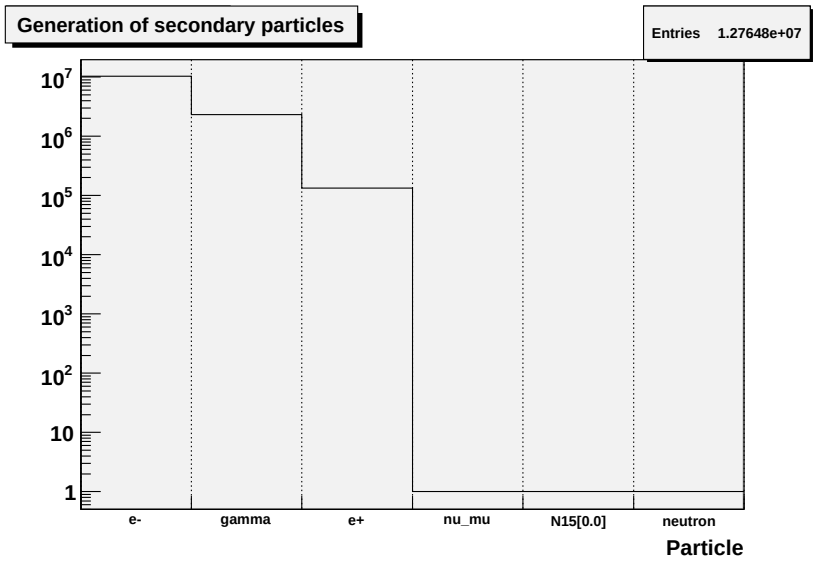

Figure 5.8: Generation of secondary particles in the detector's steel shielding created by simulation of 1000 cosmic muons (see Table 5.1).

energy deposition, a direct simulation of neutrons was preferred to another bigger simulation of cosmic muons.

5.2.1 Electron and photon signals

The high generation rates of electrons and photons strongly suggest their further inspection before focussing on fast neutrons. The start energy spectra of generated electrons and photons have not been studied before and are given in Figures 5.9 and 5.10.[6] For a better classification of the following simulation results concerning electron and photon related energy depositions, the start energies are used for an estimation of *Radiation Length* and energy loss of the particles in the steel shielding. Refering to [50], the longitudinal expansion of an electromagnetic shower can be estimated by the position of the shower maximum:

$$t^i_{max}[X_0] = \ln\left(\frac{E_0}{E_c}\right) + C_i; \qquad i = e, \gamma, \tag{5.2}$$

[6]In the simulation framework, particles with energies too small, to allow a travel distance of at least 1 mm are not generated. The energy is then directly deposited. In comparison to detector dimensions of cm, errors resulting from this cut in the simulation are negligible.

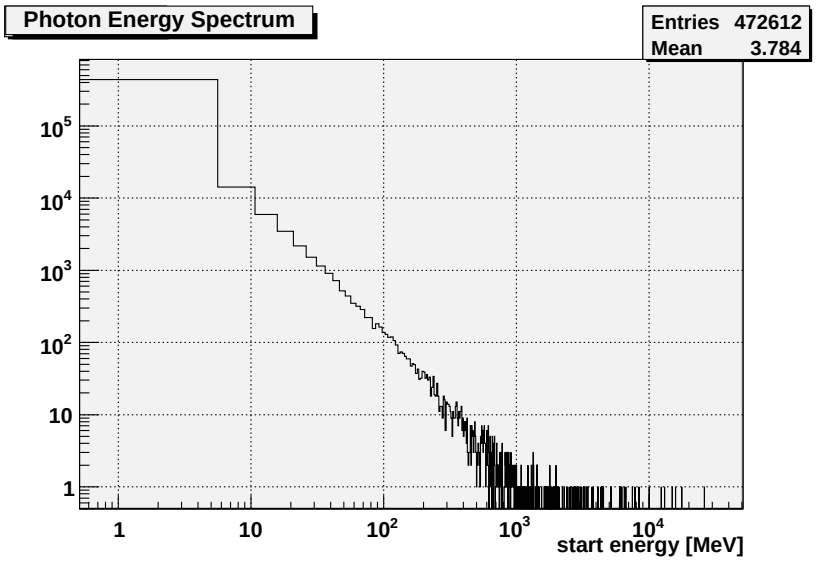

Figure 5.9: Start energy spectrum of photons created by cosmic muons in the steel shielding.

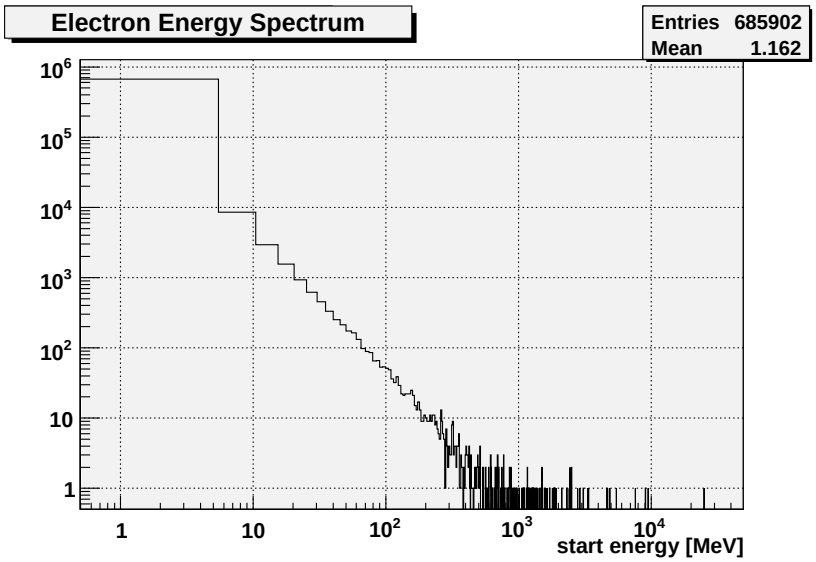

Figure 5.10: Start energy spectrum of electrons created by cosmic muons in the steel shielding.

where $t^i_{max}[X_0]$ is the position of the shower maximum in units of *Radiation Lengths*, E_0 is the start energy, E_c the *Critical Energy*, and $C_\gamma = +0.5$ (photon-induced showers), and $C_e = -0.5$ (electron-induced showers).
Electrons lose energy mainly by bremsstrahlung while photons lose energy by e^+e^- pair production. The typical amount of traversed matter for these correlated interactions is the *Radiation Length* X_0. A compact fit to existing data, illuminiating the functional dependence of X_0 from Z of the traversed matter is given by [32]:[7]

$$X_0[\mathrm{g/cm^2}] = \frac{716.4\,A}{Z(Z+1)\ln(287/\sqrt{Z})}. \tag{5.3}$$

The *Critical Energy*, being the energy at which the two loss rates of bremsstrahlung and ionization[8] of an electron are equal, can be approximated according to [51] with $E_c = (800\,\mathrm{MeV})/(Z+1.2)$.
For start energies from 10 to 1000 GeV, 98 % of the start energy are deposited within $L(98\,\%)$ [50]:

$$L(98\%) = 2.5 t^i_{max}[X_0]. \tag{5.4}$$

Treating the steel shielding as iron[9] with $Z = 26$, $A = 56$, and the density $\rho_{Fe} = 7.7\,\mathrm{gcm^{-3}}$, Table 5.2 summarizes some longitudinal expansions for different electron and photon start energies that where chosen with respect to the simulated start energy spectra. Particles with $E_0 = 10\,\mathrm{GeV}$ are very abundant and events with energies of $E_0 \simeq 100\,\mathrm{GeV}$ can be seen as an upper energy limit according to the simulation results.
The shielding has the purpose of protecting the detector from electromagnetic radiation that has its origin in nuclear processes in the surrounding rock. Therefore, steel, as a material with high density, has been chosen as a compromise between space, cost, and effectivity aspects. The executed simulation of electromagnetic showers that are generated in the shielding itself now deliver longitudinal expansions that are of the same magnitude as the thickness of the shielding (16 cm). Although the shower lengths only

[7] X_0 is caused by electromagnetic effects such as ionization and bremsstrahlung. The Coulomb potential of a nucleus increases with Z. This leads to a reduction of the *Radiation Length* for electrons and photons.

[8] Energy loss by bremsstrahlung is nearly proportional to E_e while the ionization loss rate varies logarithmically.

[9] Steel is an alloy consisting of at least 98% iron [52].

E_0[GeV]	Electron	Photon
10	24.64	29.12
100	34.72	39.76

Table 5.2: Estimation of longitudinal expansions $L(98\,\%)$ in [cm] for electronic and photonic induced electromagnetic showers in iron for different start energies E_0. After those distances, the material has absorbed 98% of the start energy. $(L(98\%)\rho_{Fe}^{-1})$.

show a logarithmic growth with increasing start energy, it becomes obvious that muon induced electromagnetic showers have a considerable probability of reaching the inner veto region of the detector, specially if produced close to the inner radius of the shielding. These observations motivate a further investigation of electrons and photons as a potential source of dangerous background in the detector.

Electrons

Table 5.3 shows the simulation results for the mean deposited energy in the detector for electrons. The size of these values displays a nearly complete suppression of average energetic particles. The dependence of the values from r is not exponential, as previous mentioned aspects would suggest. Those facts lead to the assumption that only a small amount of electrons with highest possible energies considering Figure 5.10 could be the source of potential backgrounds in the target region. Figure 5.11 shows a highest energy deposition for electrons of $\sim$30 MeV. Taking into account the thresholds of the ν-trigger being 1-10 MeV for the first energy deposition (the e^+e^--annihilation) and, in a time window of 30 μs, 2-8 MeV for the second energy deposition (the neutron capture on Gd), high energy electrons have a share in the accidental background. Table 5.3 as well as Figure 5.11 also clarify that there is, by one order of magnitude, more energy deposited in the inner veto than in the inner detector.

Photons

For photons, direct energy deposition effects in the detector are negligible. In the electromagnetic shower process, they contribute to detector backgrounds

electrons	Mean deposited energy [MeV]		
Radial distance [mm]	T+γ	T+γ+B	μ-Veto
$r_1 = 3280$	$2.012e^{-5}$	$1.025e^{-3}$	$1.047e^{-2}$
$r_2 = 3320$	$9.802e^{-6}$	$1.867e^{-4}$	$1.717e^{-3}$
$r_3 = 3360$	$2.454e^{-6}$	$6.322e^{-5}$	$3.836e^{-4}$
$r_4 = 3400$	$1.247e^{-6}$	$2.458e^{-5}$	$1.014e^{-8}$

Table 5.3: Electronic mean energy deposition in different detector areas at different muon injection points (T = Target, γ = gamma-catcher, B = Buffer).

by generation of electrons (and positrons) that are responsible for the main share of photon induced energy deposition. An analysis of direct photonic energy depositions as done for electrons in Table 5.3 and Figure 5.11 is thus not reasonable. Instead, Figure 5.12 displays the start energy spectrum of the fraction of photons that reach the inner detector area. The second histogram, showing the global energy deposition of those photons in the inner veto, now clarifies that each gamma-particle that was able to reach the buffer deposits an energy in the veto of more than 6 MeV. The value for the lower trigger threshold of the veto will be 600 photoelectrons [53]. In accordance with the gradient of the plot in Figure 5.5(b), 600 photoelectrons result in a value of ∼6 MeV as energy threshold which means that no photon will pass the veto region undetected.[10]

Consolidating those observations, it can be said that, due to their strong electromagnetic interaction, photons and electrons do not reach the target unseen by the veto. Those particles may not be regarded as a threat to the detection of neutrino signals in the Double Chooz detector within the investigated statistics.

5.2.2 Neutron signals

In contrast to the previously studied photons and electrons, neutrons are expected to show a completely different behaviour. While the former are

[10]For this investigation of photon propagation, the simulation with $r = 3280$ mm was used. Referring to the detector center, this is the closest muon input that was studied. Taking into account the strong shielding ability of the steel, muon simulations with higher $r's$ are likely to be a smaller threat to the target area.

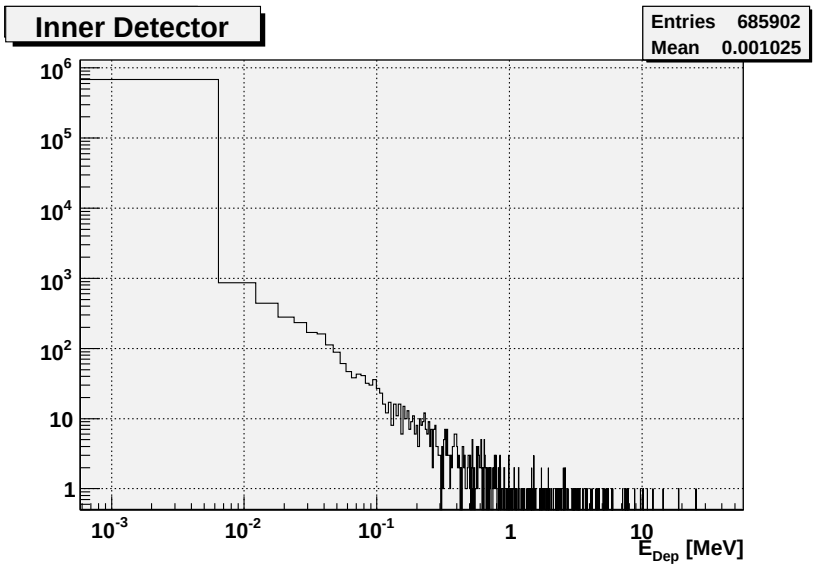

(a) Inner Detector (target+γ-catcher+buffer)

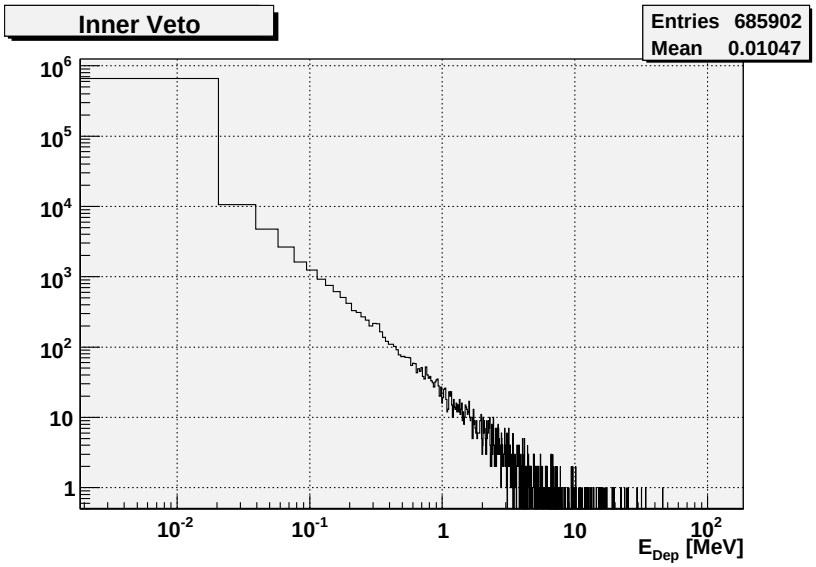

(b) Inner Veto

Figure 5.11: Deposited energy of electrons in detector areas generated by 1000 muons at $r_1 = 3280\,\mathrm{mm}$.

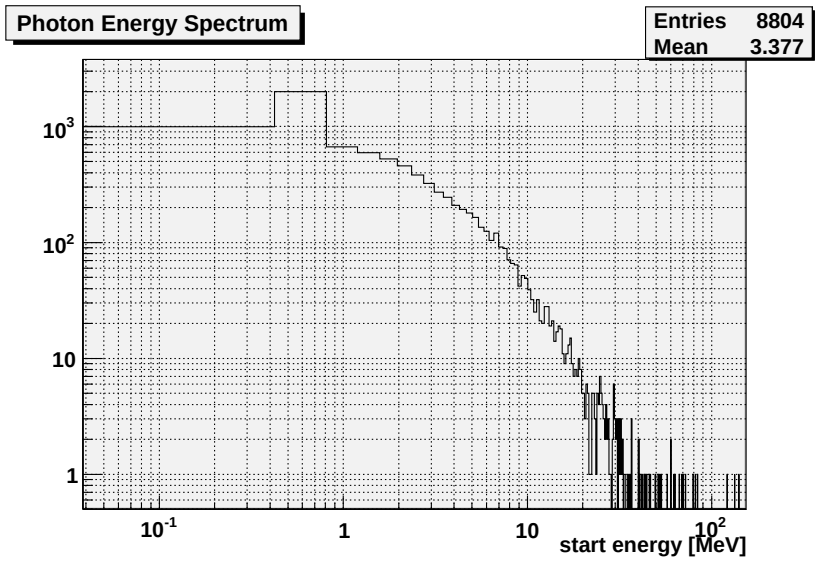

(a) Reaching the Inner Detector (target+γ-catcher+buffer)

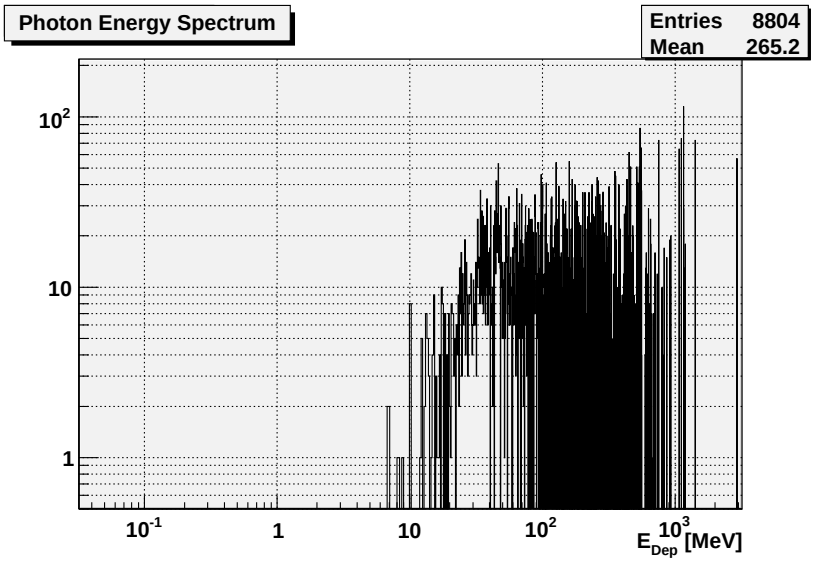

(b) Energy Deposition in Inner Veto

Figure 5.12: Start Energy Spectrum of Photons reaching the Inner Detector region and their Energy Deposition in the Inner Veto for $r_1 = 3280\,\mathrm{mm}$.

Simulated particles	n
Particle energy	$\bar{E}_0 = 321.2\,\text{MeV}$ (see Figure 5.13)
Number of particles per simulation	1000
Dimension of steel shielding	3250mm - 3410mm
Injection points	3280mm, 3320mm, 3360mm, 3400mm
Direction	Isotropic

Table 5.4: Simulation parameters for studies of fast neutron background. Parameters were chosen analogical to Table 5.1.

subject to the electromagnetic interaction with very high cross sections, neutrons are electric neutral and thus have a much higher potential of reaching the detector target area without being recognized. Nevertheless, the generation rates are much lower and it is to be examined how big their contribution is to a dangerous detector background. Due to these very low generation rates of secondary neutrons in the simulations of cosmic muons, the background of fast neutrons was simulated separately. For the sake of better comparability, the parameters for the neutron simulation were chosen similar to the simulation of cosmic muons. Table 5.4 summarizes those parameters with the only difference being the particle start energy which is now a continuous spectrum with a mean energy of 321 MeV. The neutron start energy spectrum in Figure 5.13 was created with a generator written in *C++* in accordance to a simulation of cosmic muons at the far detector with much higher statistics. This simulation was done for the DoubleChooz proposal [36]. A fit to the energy distribution of the neutrons that originated from this simulation was used as reference for the simulation with the mentioned generator and is the groundwork for the following notes.

Figures 5.14 and 5.15 illustrate start energy spectra of those neutrons that reach the inner veto and the inner detector region for $r = 3280\,\text{mm}$ and $r = 3400\,\text{mm}$ respectively. While the plots for the inner veto still show a complete spectrum of energies with dominant energies below 100 MeV, it is clearly visible that neutrons with start energies below 10 MeV do not reach the target at all. Since those lower energetic neutrons build a big fraction of the total amount in the start energy spectrum, it is helpful to see that they cannot contribute to the neutrino signal.[11] Furthermore, it proves an

[11] This statement is made for the available statistics and for four different neutron generation points.

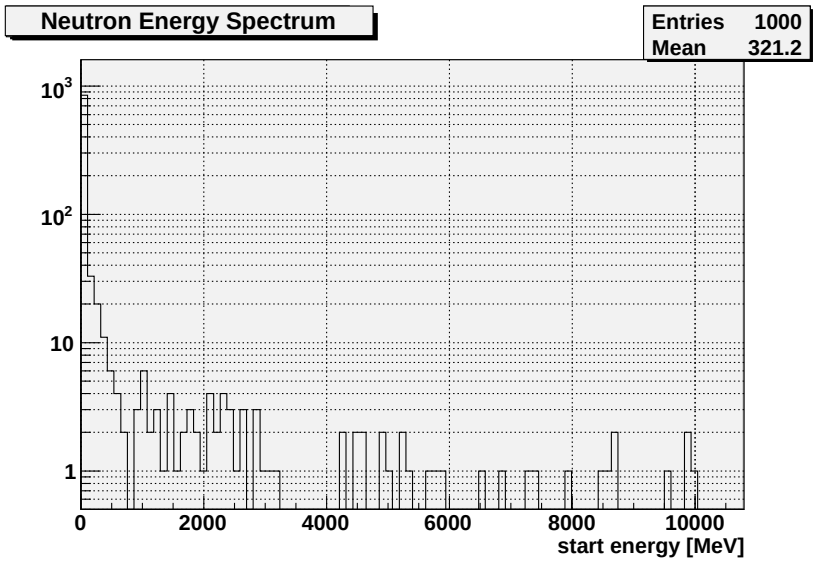

Figure 5.13: Start energy spectrum of neutrons in the steel shielding.

efficient rejection potential of inner veto and buffer. For both distances r, the total amount of observed neutrons is approximately a factor 6 lower in the detector area than in the inner veto. This is caused by recoil effects on protons and thus underlines the veto's property of being a good neutron moderator. The decrease in the total amount of entries in dependence of r once more shows the strong influence of the steel shielding on background reduction.

Like in Section 5.2.1, the mean energy deposition of neutrons for different detector areas is given in Table 5.5. As an example for the origin of those mean values, Figure 5.16 displays histograms for the energy deposition at $r = 3280\,\text{mm}$. This information clarifies the danger potential of neutrons compared to electrons and photons in terms of disturbing the neutrino detection. The deposited energy is higher in the detector area than in the veto. This means that, in contrast to electrons and photons, it must not be assumed that at this point neutrons with the ability of reaching the target area are definitely seen by the veto. The estimation of a fast neutron rate in the detector is further motivated. Besides the lower cross section of neutrons, a reason for this observation is the *Quenching Effect* of liquid scintillators. The energy deposition of particle recoil effects on atomic nuclei in the detector (eg. through neutrons) produces less light in the scintillator than the same amount of deposited energy through electromagnetic effects. Unlike

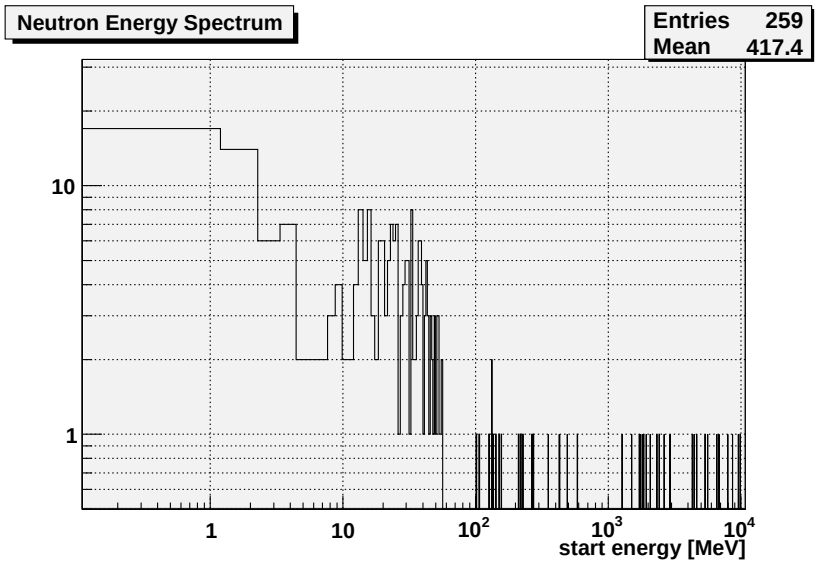

(a) Reaching the Inner Veto

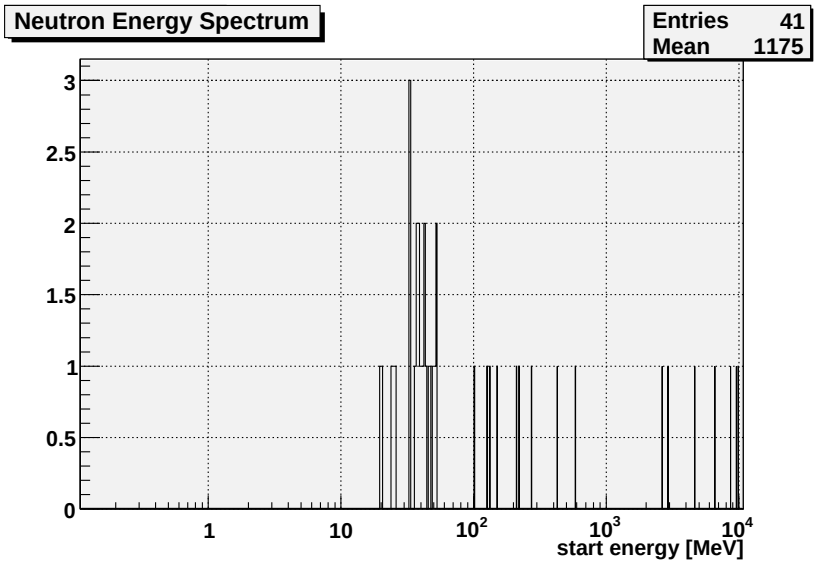

(b) Reaching the Inner Detector

Figure 5.14: Start energy spectrum of neutrons created in the steel shielding that reach different detector regions for $r = 3280\,\mathrm{mm}$.

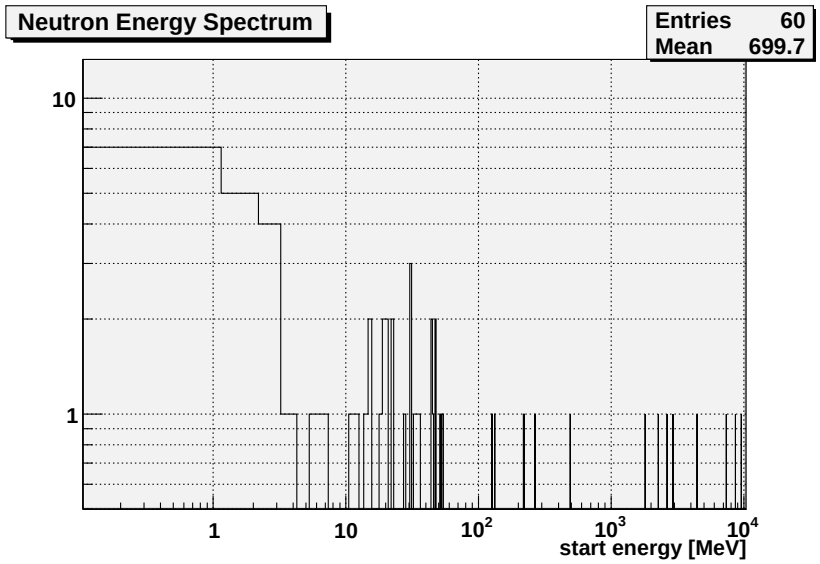

(a) Reaching the Inner Veto

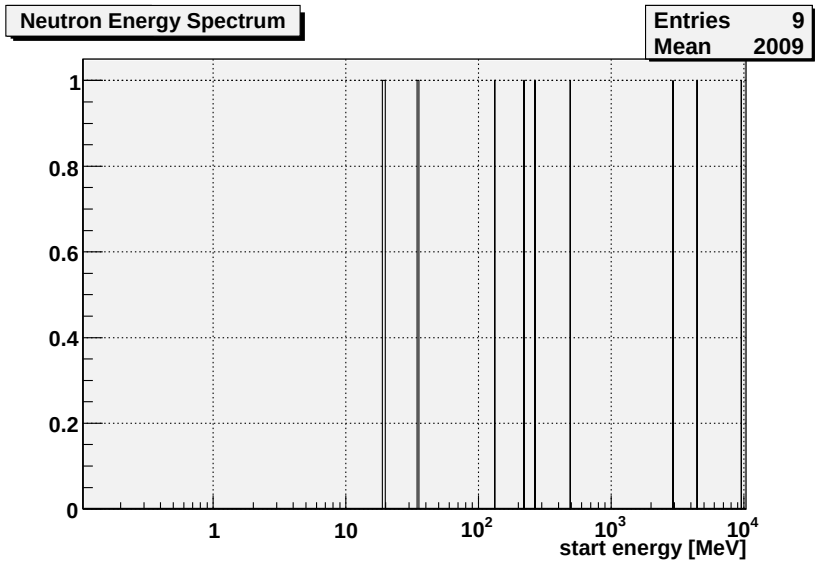

(b) Reaching the Inner Detector

Figure 5.15: Start energy spectrum of neutrons created in the steel shielding that reach different detector regions for $r = 3400\,\mathrm{mm}$.

neutrons	Mean deposited energy [MeV]		
Radial distance [mm]	T+γ	T+γ+B	μ-Veto
3280	12.85	48.08	36.87
3320	9.19	34.98	31.42
3360	9.06	30.49	24.23
3400	5.23	25.71	14.72

Table 5.5: Neutron mean energy deposition in different detector areas at different neutron injection points (T = Target, γ = gamma-catcher, B = Buffer).

neutrons, electromagnetic particles like electrons and photons interact with the electronic cloud of the target atoms which results in a much higher light efficiency.[12] The *Quenching Factor* is introduced as a quantitative measure that describes this effect by giving a value for the reduction of neutron light efficiency compared to electrons and photons. This factor is dependent on charge, mass, and energy of the involved particles and on scintillator specific parameters [54]. For neutron recoil on protons in the DoubleChooz liquid scintillator detector, it will be about 10. The neutron capture on Gd that takes place in the target area releases a fixed amount of energy of $\simeq 8\,\mathrm{MeV}$. It is independent from the *Quenching Factor*. This fixed energy has a relatively bigger share in the lower values of the measured mean energy depositions. Therefore, those lower values are less dependent on the *Quenching Factor* that reduces only the non-fixed part of the energy deposition. Nevertheless, the range of deposited energy in the histogram falls well within the signal window for neutrino events of between 1 and 10 MeV.

As opposed to the theoretical value of the deposited energy, the visible energy (E_{Vis}) is a parameter that simulates the amount of energy that is actually detectable by the detector and includes experimental factors like the *Quenching Effect*. In Figures 5.17 and 5.18, scatter plots are drawn opposing the visible energy in the inner veto to the visible energy in the inner detector for the simulated 1000 neutrons at different distances r. A focus is made on the energy sectors in which neutrons have the ability of disturbing the neutrino detection. Neutrons that put a visible energy of less than 6 MeV into the veto lie below the trigger threshold and will remain undetected.

[12] Heavier electromagnetic particles like p and α can do both an excitement of the electron cloud and a recoil on the atomic nucleus.

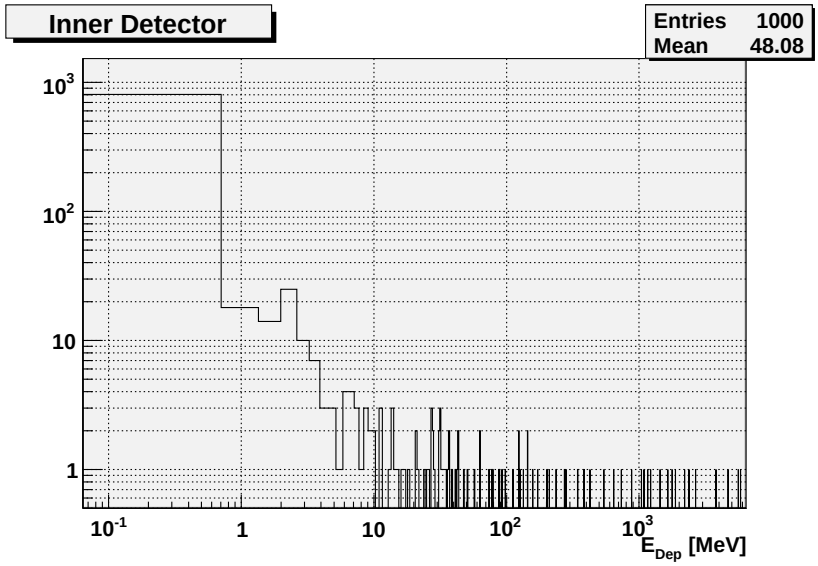

(a) Inner Detector

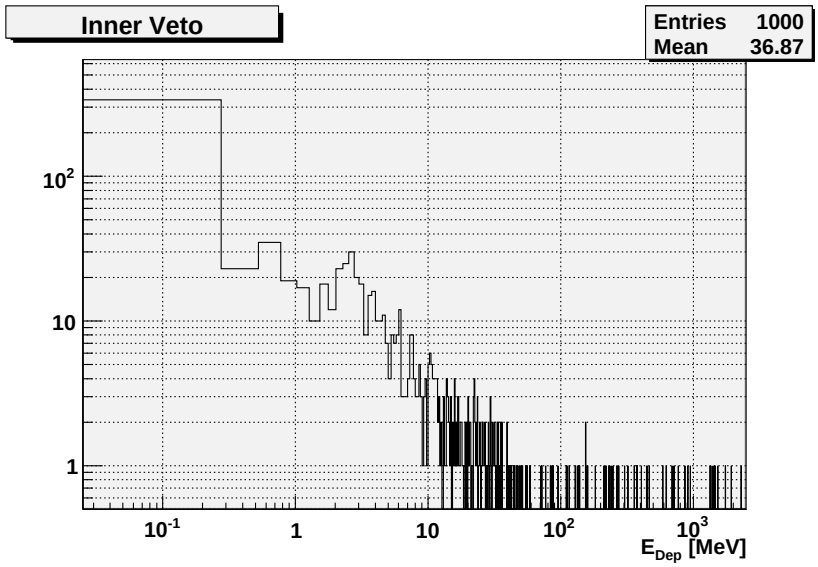

(b) Inner Veto

Figure 5.16: Deposited energy of neutrons in detector areas for $r = 3280\,\mathrm{mm}$.

r [mm]	# of n
3280	5
3320	1
3360	5
3400	1

Table 5.6: Number of "neutrino-like" neutrons (out of 1000 simulated ones) for different injection points r.

Those particles can cause a visible energy in the range of 1-10 MeV in the inner detector and therefore contribute to accidental or even to correlated background by mimicking the signal of an antineutrino.[13] A closer look at the scatter plots reveals that a dependence of the amount of those neutrons on r is not verifiable. An availability of much higher statistics might change this observation, but for the following estimation of a rate for the fast neutron background, a constant behaviour is assumed for the dimension of the steel shielding. This will lead to a conservative estimation of the background rate.

Table 5.6 summarizes the neutron numbers that result in a mean value of 3 ± 2.3 neutrons.[14] Their share in the total amount of 1000 simulated neutrons is $0.30 \pm 0.23\,\%$. Now, to achieve the aim of finding a rate for the fast neutron background, additional information is required. A simulation that was done fot the DoubleChooz proposal [36] predicts a muon flux of $\Phi_\mu = 6.2 \cdot 10^{-5}\,\mathrm{cm^{-2}s^{-1}}$ for the far detector considering the topographical structure of the rock overburden. Applied on the ring area[15] of the steel shielding of $A = 33476.8\,\mathrm{cm^2}$, the muon rate through the steel shielding is $N_{\mu,steel} = \Phi_\mu \cdot A = 2.08\,\mathrm{s^{-1}}$. The next step is to calculate the number of neutrons produced by a cosmic muon travelling through the steel shielding. Equation (2.31) can be used. The relevant mean muon energy of $E_\mu = 63\,\mathrm{GeV}$ that was used for the previously performed simulation is inserted. Futhermore, the density of iron $\rho_{Fe} = 7.7\,\mathrm{gcm^{-3}}$ as approximation for steel (see Section 5.2.1) and the height of the shielding ring $h = 700\,\mathrm{cm}$ as extent for the muon travelling distance are used. This results in the value of $N_n = 0.48\,\mathrm{neutrons}/\mu$ for the steel shielding of the DoubleChooz far detector. Multiplication with

[13] Neutrons with such characteristics will be called "neutrino-like".

[14] With an statistical error of almost 100 %, this value must be treated carefully. It should be interpreted as a guidance value for the magnitude of the number of "neutrino-like" neutrons.

[15] $A[\mathrm{cm^2}] = \pi(r_{out}^2 - r_{in}^2)$ with $r_{out} = 341\,\mathrm{cm}$ and $r_{in} = 325\,\mathrm{cm}$

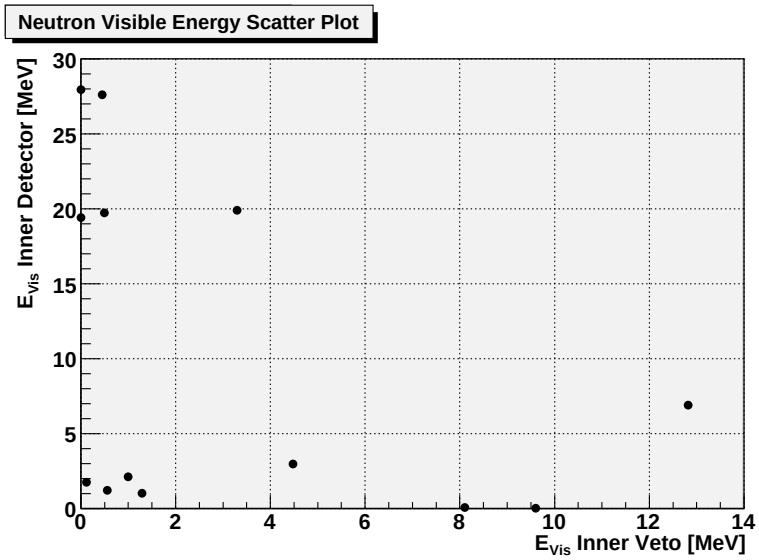

(a) $r = 3280\,\mathrm{mm}$

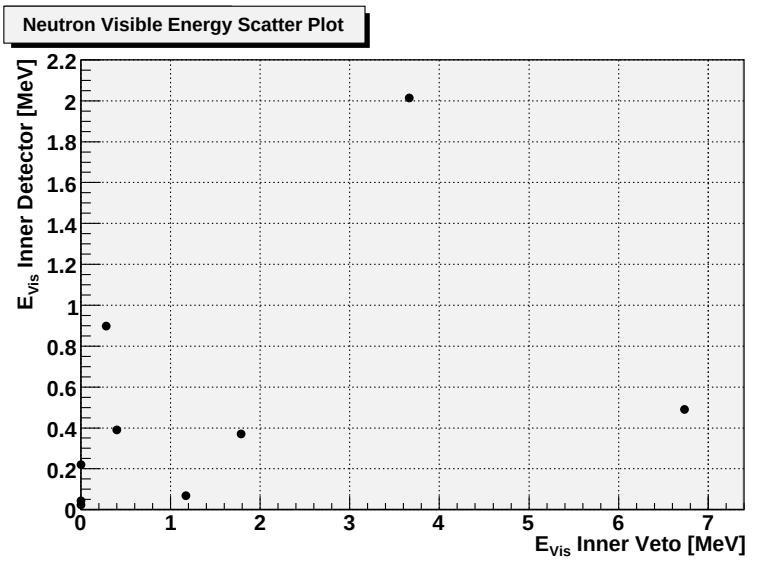

(b) $r = 3320\,\mathrm{mm}$

Figure 5.17: Scatter plots of visible energy depositions in veto and target areas for different neutron injection points (r). Out of the 1000 entries, a cut is done on energies with $E_{Vis} < 20\,\mathrm{MeV}$ in the veto and $0 < E_{Vis} < 40\,\mathrm{MeV}$ in the target region (target + γ-catcher + buffer).

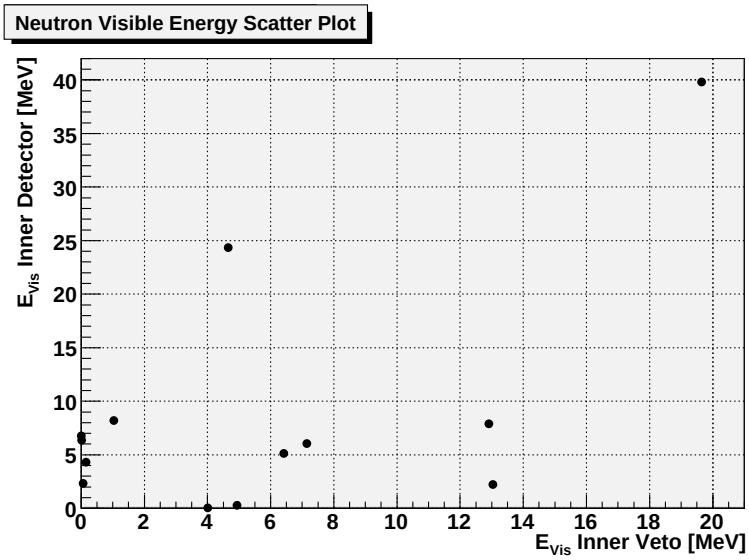

(a) $r = 3360\,\mathrm{mm}$

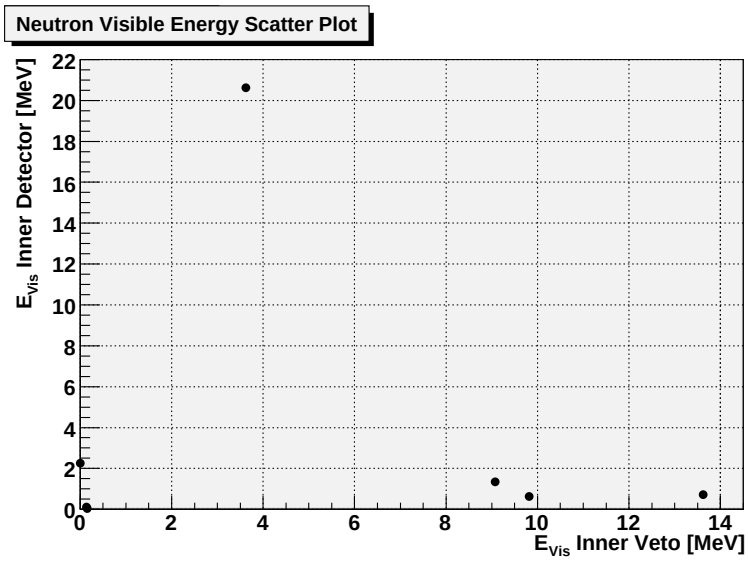

(b) $r = 3400\,\mathrm{mm}$

Figure 5.18: Continued scatter plots.

$N_{\mu,steel}$ gives an expected neutron rate of $R_n = 1.00\,\mathrm{s}^{-1}$. Hereof, a percentage of $0.30 \pm 0.23\,\%$ has the ability of producing a "neutrino-like" signal. The rate of these neutrons is hence $R_n = 3.0 \pm 2.3 \cdot 10^{-3}\,\mathrm{s}^{-1}$ or $R_n = 259 \pm 199\,\mathrm{d}^{-1}$. As mentioned above, the simulation results do not show a significant decrease of "neutrino-like" neutrons with increasing distance of muon injection r. In [55] a FLUKA[16] simulation of fast neutrons in rock was performed for the DoubleChooz detector geometry. A radial distance of $r_0 = 4\,\mathrm{m}$ was found as limit for neutrons that have the ability to reach the detector volume. In order to take this additional area into account as well, the calculation of R_n can be repeated for the ring area consisting of rock reaching from the outer limit of the steel shielding to the distance of 4 m. This leads to a rate of $R_{n,2} = 384 \pm 199\,\mathrm{d}^{-1}$. This estimation is again very conservative as no influence of the increasing distance of neutron generation is assumed at all. Therefore the result of a combined rate $R_n + R_{n,2} = 643 \pm 199\,\mathrm{d}^{-1}$ must be regarded as an upper limit.
For the near detector, the previous calculation yields a combined rate of $R_{n,near} + R_{n,2,near} = 2138 \pm 199\,\mathrm{d}^{-1}$. The lower rock overburden causes a different muon rate and a different mean muon energy at the near detector site.

Obviously, this result does not meet the requirements for reaching a signal to noise ratio of 100 (see Table 3.3), but another effect must be considered:

Correlation constraint

In order to become a threat to the experiment, fast neutrons must imitate the two correlated signals of a neutrino event. That means they not only have to be captured on Gd, releasing the right amount of energy after undetected transit through the inner veto, but also they have to emit gamma-radiation according to the e^+e^--annihilation induced by the inverse β-decay in a time window before the capture. The very typical neutrino detection signature is therefore supposed to further reduce the rate of dangerous neutrons.
The reduction of the rate because of this timing effect is now studied in the simulation environment for the first time [53]. A macro was written in $C++$ with the following functionality. For each of the simulated neutron events, the produced photoelectrons of all PMT's in the inner detector are put into

[16] **FLU**ktuierende **KA**skade. A Monte Carlo simulation package for the interaction and transport of particles and nuclei in matter.

bins with a width of 100 ns.[17] Then, it is searched for points in time with a production of more than 100 photoelectrons. According to Section 5.1.1, this corresponds to 0.6 MeV of produced energy and is a conservative selection of a trigger threshold. These points of time are now compared with each other. It is searched for two of them with a time difference between 10 and 100 μs that would be counted as a neutrino signature. Moreover, the number of produced photoelectrons in the inner veto is monitored for those events. If the number of photoelectrons is above 1000, the event will be treated as seen by the veto.
An application of this macro on the 4000 simulated neutron events ($4 \cdot 1000$ events at 4 different distances; Table 5.4) results in 0 "neutrino-like"[18] signals within the critical time window. Figure 5.19 provides an example of a neutrino-like event that does not contribute to the correlated background. None of the 12 events, that were interpreted as "neutrino-like", meet the additional constraint. These observations allow the assumption of an additional factor of at least 10, suppressing the rate of correlated fast neutron background. The importance of the typical delayed detection signature of the inverse β-decay as a method to distinguish neutrinos from background effects becomes obvious.

[17] Compared to the read-out time of the used Flash-ADC's of 256 ns, the binning size of 100 ns does not produce an additional inaccuracy.
[18] As defined before.

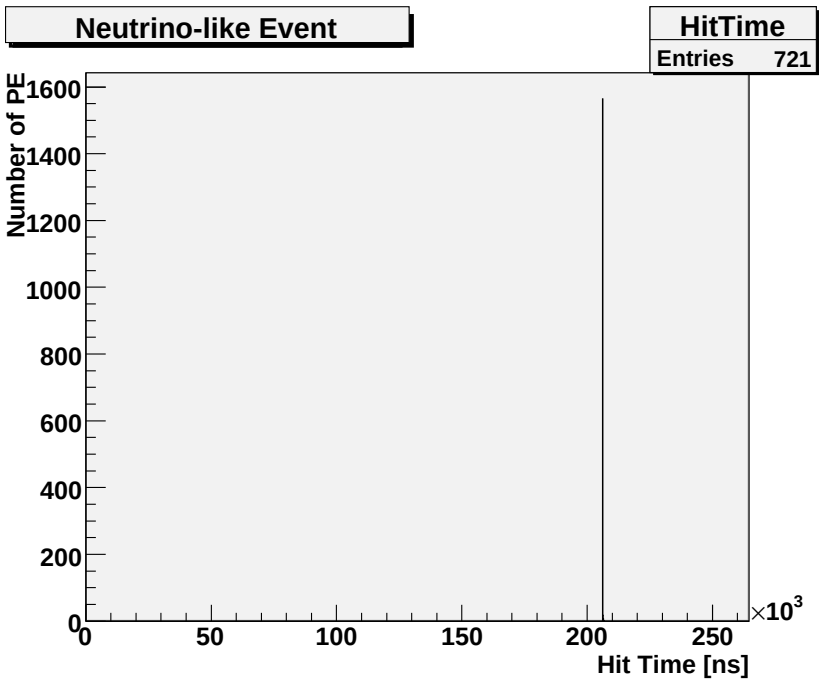

Figure 5.19: Example analysis of one "neutrino-like" event.
This is an event from Figure 5.18(a) with E_{Vis} Inner Veto $\approx 1\,\mathrm{MeV}$ and E_{Vis} Inner Detector $\approx 8\,\mathrm{MeV}$. After a living time of $\approx 208\,\mu s$, 721 PMT-hits produce ≈ 1600 photoelectrons. Taking into account the observed value of $\approx 178\,\mathrm{PE/MeV}$, this corresponds to an energy deposition of more than 8 MeV and suggests a capture on Gd. However, no second energy deposition in the critical time window before the Gd-capture is observed. Therefore, this event does not mimic a neutrino signal. It is rejected by the correlation constraint.

Chapter 6

Summary and Outlook

The field of neutrino physics belongs to the most promising branches of modern particle physics. A deeper understanding of effects beyond the SM such as neutrino oscillations can significantly extend the knowledge about our universe and its origin. In the context of neutrino oscillation experiments, DoubleChooz will contribute to the determination of the only still unknown mixing angle θ_{13}. For future experiments, this may provide access to an undisturbed search for the CP-violating phase in the neutrino oscillation mechanism. Due to the extremely small cross section of neutrinos, oscillation experiments have to cope with low detection rates. In order to obtain an acceptable signal to noise ratio, an effective background rejection is therefore crucial to the success of DoubleChooz.

In this work, the GEANT4-based simulation software package DOGS was installed and used to study background effects induced by cosmic muons in the steel shielding of the DoubleChooz detector. In the simulation, the muons were approaching vertically with a mean energy that resulted from the previous passage of the rock overburden.
An exponential decrease of the total amount of energy deposited in the inner detector (target, γ-catcher, buffer) and the inner veto with increasing radial distance of muon injection was observed. This effect is in accordance with the general absorption law. Also, a linear relation between deposited energy and production rate of photoelectrons in the photomultipliers was identified. The results for the inner veto are in very good agreement with linearity. For the inner detector, statistical issues caused stronger deviations from linearity. Furthermore, the expected production rate of photoelectrons of 180 per

MeV could be confirmed within the statistics. With this, a cross check of the functionality of the simulation software was performed.
For the first time, implications of the PMT alignment on the efficiency of photoelectron production were investigated. The alignment of the inner veto PMT's in vertical rows each 30 degrees could be visualised with simulations that were done in a circle of muon-injection points each 15 degrees. For the number of produced photoelectrons, deviations of about 15 % from the mean value were observed in both directions. The inner detector PMT's are aligned in vertical rows each 12 degrees. While a periodic behaviour, similiar to the inner veto, was not obvious, a dependence of the photoelectron yield on the place of muon injection became clear.
The next step was to study the particle-wise contributions to the detector background. An estimation of the radiation lengths of electromagnetic showers in the steel shielding for different energies demonstrated their ability to reach the detector areas inside the shielding. While the steel provides an effective rejection of radiation that is generated in the surrounding rock, muon induced electrons and photons with origin in the shielding itself turned out to be a source of potential background. For this reason, deeper studies were performed. The statement could be made that both electrons and photons with the ability of reaching the inner detector are completely monitored by the inner veto. A threat to neutrino detection caused by electrons and photons could therefore be rejected within the statistics.
To efficiently study neutron events as a source of correlated background, a dedicated simulation was performed. Fast neutrons were simulated directly in accordance with an expected energy spectrum at the far detector site. It was shown that neutrons with a start energy of below 10 MeV cannot reach the inner detector at all. The steel shielding, the inner veto, and the buffer all contribute to the decrease of the neutron rate in the target area. The higher energy deposition in the inner detector was explained. After those observations, scatter plots were drawn in order to reveal neutrons with the potential of mimicking the typical correlated signal of a neutrino event. In this way, 12 neutrons (out of 4000) were found that deposited a characteristic energy of between 1 and 10 MeV in the inner detector without being previously detected by the inner veto. In combination with additional information, this number was used to estimate a rate of neutrons with the potential of being detected as neutrino signal. This rate is $2138 \pm 199\,\mathrm{d}^{-1}$ for the near detector and $643 \pm 199\,\mathrm{d}^{-1}$ for the far detector. Further studies on these rates

were done concerning the additional time correlation constraint. Out of the simulated 4000 neutrons, no neutron caused two energy depositions within the time window of the typical neutrino signature. Decreasing the number of neutrons that can emulate a neutrino signal from 12 to 0, this constraint yields a suppression factor of the neutron rate of at least 10.

In the frame of this work, it has been shown that it is quite challenging to achieve a signal to noise ratio of 100 in the DoubleChooz experiment. Particularly the behaviour of fast neutrons can be a source of correlated background. For future investigations, it is recommended to significantly increase the statistics in the simulations of cosmic muons. This would allow a direct analysis of muon induced neutrons without separate simulations of neutrons themselves. In order to confirm the expected signal to noise ratio, the neutron data set should be enlarged by a factor of 100. As a next step, the vertical approaching direction of the simulated muons could also be replaced by an angular distribution corresponding to the topography at the detector site.

Appendix A

A brief Software Guideline

This appendix successively explains the steps to be performed to get to the desired simulation results. A working installation of the DOGS software package is a prerequisite. For an installation tutorial, please refer to the Double Chooz Webpage [43].

A.1 Running a Simulation

Before starting a simulation, a bunch of environmental variables have to be defined in order to align the shell with the DCGLG4sim functionalities. The Double Chooz collaboration website mentions all needed variables during the installation tutorial. Figure A.1 provides a summary of the needed variables.

The execution of a simulation requires a macro-file that determines all input information. In most cases, these macros do not have to be written from scratch. The folder *DOGS/DCGLG4sim/mac* contains a lot of detailed example macros serving as good templates for particle simulations of all kinds. The source code is often extensively explained. Table A.1 summarizes some of the most crucial input commands.

Once the macro is written, the simulation can be started. The command *dcglg4sim mac/macrofilename.mac* launched in the *DOGS/DCGLG4sim* folder executes the simulation.
The resulting data will be stored in *DOGS/DATA* in *ROOT*-format. Here, a seperation into three data files (*filename_base.root, filename_part.root, filename_track.root*) takes place. How to deal with those files is explained in the following Section A.2.

Command	Description
/glg4debug/glg4param omit_hadronic_processes 1.0	Deactivate hadronic processes (Many other parameters of *settings.dat* and *settings_cylindrical.dat* in the folder *DOGS/DCGLG4sim/data* can be changed respectively.)
/output/store/particles 1	store information about every particle (huge output files) setting it to 0: no information will be stored uncommenting it with #: primary particles will be stored (default)
/output/store/tracks 1	the same as above for particle tracks
/run/initialize	initialize geometry
/process/inactivate Cerenkov	inactivates Cerenkov light (results in decrease of simulation running time)
/glg4scint/off	inactivate photons (also huge speed up, but completely ignores scintillation processes and the resulting photoelectrons
/generator/gun mu- x y z p_x p_y p_z E	Simple test gun defining particle type (μ^-), starting location (xyz) starting momentum ($p_x p_y p_z$) and starting energy (E[MeV]). This is the most basic way of introducing primary particles. Alternatively, data files with pre-simulated spectra of particle energies and angles eg. using the MUSIC tool (Section 4.2.3) can be used as a more sophisticated and precise starting point.
/event/output_file filename	Sets filename for output file that is stored in *DOGS/DATA*.
/run/beamOn n	n is the number of events to be simulated.

Table A.1: Basic simulation input commands.

```
export CVS_RSH=ssh
export CVSROOT=tlammers@cvs.in2p3.fr:/cvs/dchooz
export ROOTSYS=/opt/products/root/5.14.00
export PATH=$ROOTSYS/bin:$PATH
export LD_LIBRARY_PATH=$ROOTSYS/lib:$LD_LIBRARY_PATH
export G4INSTALL=/rdata/uh2iexpfs1/opera/chooz/geant4/geant4.8.3
export G4SYSTEM=Linux-g++
source $G4INSTALL/.config/bin/$G4SYSTEM/env.sh
export G4WORKDIR=/rdata/uh2iexpfs1/opera/chooz/work/$USER/
export PATH=$G4WORKDIR/bin/$G4SYSTEM:$PATH
export LD_LIBRARY_PATH=$G4WORKDIR/tmp/$G4SYSTEM:$LD_LIBRARY_PATH
export DOGS_PATH=/rdata/uh2iexpfs1/opera/chooz/tlammers/DOGS/
export PATH=$DOGS_PATH/bin:$PATH
export LD_LIBRARY_PATH=$DOGS_PATH/lib:$LD_LIBRARY_PATH
```

Figure A.1: Example set of environmental variables to be engaged each time a new shell is used for executing simulations. It is recommended to summarize them in one executable batch-file. This *file.sh* then has to be launched with *source file.sh* prior to a new simulation.

- *filename_base.root*
  Basic output file that provides simulation information directly comparable to real experimental results. It covers PMT and E_{Dep} information for all volumina and particles similar to the actual detector response.

- *filename_part.root*
  Detailed information about each single particle produced in the interaction process such as starting data (E, p, t), point of creation, charge, name and summarized track information.

- *filename_track.root*
  Precise track information of each particle allowing geometrical reconstruction and display of each interaction point. Energies and kind of interaction (scattering etc.) can be observed.

Sometimes it can be more efficient to run several simulations simultaneously. Big, long lasting simulations should be subdivided into several smaller simulations[1]. Hence the risk of a collapse and the amount of data possibly lost is decreased significantly.[2] In the data analysis the seperated data can

[1]For instance, the results of a simulation of n cosmic muons can also be obtained by executing k identical simulations covering n/k primary particles each.

[2]In DCGLG4sim, a generator automatically varies the random numbers that are taken as starting point for the Monte Carlos. Therefore, there is no danger of obtaining exactly

be re-combined easily. Running several simulations at a time can be facilitated by using the *screen*-command of the Linux-shell providing the ability to supervise many simulations in one shell-window.[3]

A.2 Data Analysis

ROOT is the tool to use for Data Analysis and Release. For a detailed description of the *ROOT* functionalities, refer to the *ROOT* Manual [46]. While most of the examinations can be done using *ROOT*'s graphical interface, the TBrowser, very complex problems require the macro-based DOGS-package DCAna. The TBrowser enables the user to work within the *ROOT* software in a simplified way. Instead of typing commands, drag&drop can be used in many cases. For starting the TBrowser in *ROOT*, it is recommended to follow the commands in Figure A.2. Nevertheless, the *TBrowser a* opens without any pre-definitions. In this case, one will have to browse for the desired Data file and to manually open the Viewer by right-clicking on the GlobalThInfo folder afterwards.

Once in the viewer mode, Data analysis and creation of diagrams can easily be done. The different data sets provided by the output file of DCGLG4sim, that is now loaded into *ROOT*, are displayed as leaves in the Viewer (see Figure A.3) and can be dragged & dropped to the diagram axes as well as to the scissors symbol for setting cuts. The following list briefly summarizes the most important leaves and their contents:

- *fEventID*
  Energy deposition number (upon trigger assessment on data) from run start.
  Used as a cut, this function can highlight the contribution of one single certain event of a simulation.

- *fNParticles*
  Number of particles produced in this event

the same results for each run when executing several partial simulations with the same input parameters.

[3] All statements refer to the software version of the DOGS package downloaded on 4 July 2007.

```
gStyle->SetPalette(1,0);
gStyle->SetPadColor(0);
TChain *GTIC = new TChain("GlobalThInfoTree");
TChain *ParTIC = new TChain("ParticleThInfoTree");
GTIC->Add("DCInfoTree_MCG4_v4_filename_base.root");
ParTIC->Add("DCInfoTree_MCG4_v4_filename_part*.root");
GTIC->AddFriend("ParticleThInfoTree");
GTIC->StartViewer();
```

Figure A.2: This set of commands opens *ROOT*'s TBrowser in Viewer mode in the last command line. The commands before enable the TBrowser to process and display Data sets from different DCGLG4sim output files at once. In this example, all the information stored in the *_base* file and the *_part* files are taken into account. This allows the creation of sophisticated diagrams comparing global and particle-related data. As the part file is, due to its size, automatically split into several files, the * symbol in command line 6 becomes necessary. (It is recommended to save these commands in a text file and copy-paste them if needed.)

- *fNPhotons*
  Number of photons generated in this event

- *fEdep[]*
  Deposited Energy by primary particles
  [MeV]
  Different Volumina can be adressed with the numbers 0-6 in the brackets. (1=Target, 2=γ-catcher, 3=Buffer, 4=Inner Veto, 5=Outer Veto, 6=Inactive Volumina, 0=Σ1-6).

- *fQPE*
  Total number of photoelectrons
  To get a result here, obviously scintillation has had to be switched on in the simulation.

- *fQPEinV*
  Number of photoelectrons in inner vessel
  inV = Target + γ-catcher + Buffer.

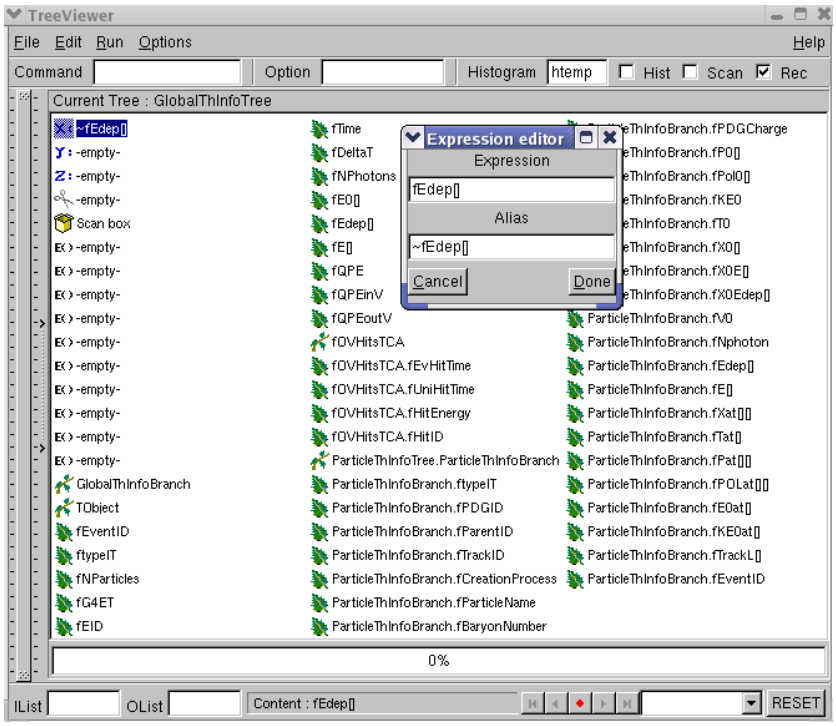

Figure A.3: The screenshot shows the working environment provided by the Viewer of the TBrowser.

- *fQPEoutV*
  Number of photoelectrons in outer vessel
  outV = Inner μ-veto.

- *fDeltaT*
  Time elapsed since last event (by Geant4)
  [ns]

- *ParticleThInfoBranch.fPDGID*
  Particle code numbers as defined from PDG
  Very useful for cuts. (eg. an edited expression with . . . ==2112 restricts the analysis to neutrons only).

- *ParticleThInfoBranch.fParentID*
  Connection between particle and its parent
  Interesting option for analysis macros: How many of the visible photons were generated in neutron reactions?

- *ParticleThInfoBranch.fCreation Process*
  Creation process of particle generation
  Was the particle generated through elastic or inelastic scattering?
  The expression has to be completed with .fDATA. (The same for *.fParticleName*)

- *ParticleThInfoBranch.fkE0*
  Kinetic Energy of primary particle at start
  Useful for creation of energy spectra in case the primary particles did not start with a pre-defined kinetic energy.

Leaves starting with *f* belong to the *_base*-file and give information about effects of all simulated particles. Leaves starting with *ParticleThInfoBranch.f* belong to the *_part*-file and refer to single-particle-properties. Some data sets appear in both files and are not listed twice here. (For instance *f.Edep* shows an average deposited energy as an integral over all participating particles whereas *ParticleThInfoBranch.fEdep* provides information about the deposited energy of each single particle respectively.) A right-click on a leave opens a menu in which you can edit its expression.

Bibliography

[1] Steven Weinberg. A Model of Leptons. *Phys. Rev. Lett.*, 19:1264–1266, 1967.

[2] C. Berger. Elementary particle physics: From the foundations to the modern experiments. Berlin, Germany: Springer (2006) 496 p.

[3] C. Grupen. Astroparticle physics. Berlin, Germany: Springer (2005) 441 p.

[4] N. Schmitz. Neutrino physics. (in german). Stuttgart, Germany: Teubner (1997) 478 p.

[5] K. Zuber. Neutrino physics. Bristol, UK: IOP (2004) 438 p.

[6] Boris Kayser. Neutrino physics. 2005. hep-ph/0506165.

[7] Minako Honda, Yee Kao, Naotoshi Okamura, and Tatsu Takeuchi. A simple parameterization of matter effects on neutrino oscillations. 2006.

[8] G. Mention. *Étude des sensibilités et bruits de fond de l'expérience Double Chooz pour la recherche du paramètre de mélange leptonique* θ_{13}. PhD thesis, University Claude Bernard, Lyon.

[9] H. Minakata, H. Sugiyama, O. Yasuda, K. Inoue, and F. Suekane. Reactor measurement of theta(13) and its complementarity to long-baseline experiments. *Phys. Rev.*, D68:033017, 2003.

[10] W. Pauli. Dear radioactive ladies and gentlemen. *Phys. Today*, 31N9:27, 1978.

[11] F. Reines and C. L. Cowan. Detection of the Free Neutrino. *Nature*, 178:446–449, Sep 1956.

[12] C. S. Wu, E. Ambler, R. W. Hayward, D. D. Hoppes, and R. P. Hudson. Experimental test of parity conservation in beta decay. *Phys. Rev.*, 105:1413–1414, 1957.

[13] M. Goldhaber, L. Grodzins, and A. W. Sunyar. Helicity of neutrinos. *Phys. Rev.*, 109:1015–1017, 1958.

[14] G. Danby, J-M. Gaillard, K. Goulianos, L. M. Lederman, N. Mistry, M. Schwartz, and J. Steinberger. Observation of High-Energy Neutrino Reactions and the Existence of Two Kinds of Neutrinos. *Phys. Rev. Lett.*, 9(1):36–44, Jul 1962.

[15] *The DONUT experiment: First direct evidence of nu/tau*, 2000. Prepared for 28th SLAC Summer Institute on Particle Physics: Neutrinos from the Lab, the Sun, and the Cosmos (SSI 2000), Stanford, California, 14-25 Aug 2000.

[16] D. Buskulic et al. Z production cross-sections and lepton pair forward - backward asymmetries. *Z. Phys.*, C62:539–550, 1994.

[17] P. Abreu et al. Improved measurements of cross-sections and asymmetries at the z0 resonance. *Nucl. Phys.*, B418:403–427, 1994.

[18] M. Acciarri et al. Measurement of cross-sections and leptonic forward - backward asymmetries at the z pole and determination of electroweak parameters. *Z. Phys.*, C62:551–576, 1994.

[19] R. Akers et al. Improved measurements of the neutral current from hadron and lepton production at lep. *Z. Phys.*, C61:19–34, 1994.

[20] K. Eguchi et al. A high sensitivity search for anti-nu/e's from the sun and other sources at kamland. *Phys. Rev. Lett.*, 92:071301, 2004.

[21] K. Eguchi et al. First results from kamland: Evidence for reactor anti-neutrino disappearance. *Phys. Rev. Lett.*, 90:021802, 2003.

[22] T. Araki et al. Measurement of neutrino oscillation with kamland: Evidence of spectral distortion. *Phys. Rev. Lett.*, 94:081801, 2005.

[23] Vernon D. Barger et al. Neutrino decay and atmospheric neutrinos. *Phys. Lett.*, B462:109–114, 1999.

[24] Yuval Grossman and Mihir P. Worah. Atmospheric nu/mu deficit from decoherence. 1998.

[25] M. Shiozawa. Super-kamiokande: Experimental results and future possibilities of atmospheric neutrino measurements. *Prog. Part. Nucl. Phys.*, 57:79–89, 2006.

[26] T. Kajita. Results from solar, atmospheric and k2k experiments and future possibilities with t2k. *Pramana*, 67:639–654, 2006.

[27] M. Apollonio et al. Search for neutrino oscillations on a long base-line at the chooz nuclear power station. *Eur. Phys. J.*, C27:331–374, 2003.

[28] Y. Fukuda et al. Atmospheric muon-neutrino / electron-neutrino ratio in the multigev energy range. *Phys. Lett.*, B335:237–245, 1994.

[29] Toshiyuki Toshito. Super-kamiokande atmospheric neutrino results. 2001.

[30] M. Apollonio et al. Limits on neutrino oscillations from the chooz experiment. *Phys. Lett.*, B466:415–430, 1999.

[31] S. A. Dazeley. Double chooz: Optimizing chooz for a possible theta(13) measurement. *Nucl. Phys. Proc. Suppl.*, 155:227–228, 2006.

[32] W. M. Yao et al. Review of particle physics. *J. Phys.*, G33:1–1232, 2006.

[33] H. Wulandari. *Study on Neutron-Induced Background in the Dark Matter Experiment CRESST*. PhD thesis, Technische Universitat Munchen, 2003.

[34] F. F. Khalchukov et al. Hadrons and other secondaries generated by cosmic ray muons underground. *Nuovo Cim.*, C18:517–529, 1995.

[35] Y. F. Wang et al. Predicting neutron production from cosmic-ray muons. *Phys. Rev.*, D64:013012, 2001.

[36] F. Ardellier et al. Double chooz: A search for the neutrino mixing angle theta(13). 2006.

[37] F. Ardellier et al. Letter of intent for double-chooz: A search for the mixing angle theta(13). 2004.

[38] V.V. Sinev. Present status of double chooz experiment. Physics of atomic nuclei, Vol. 69, No. 11, 2006.

[39] A. Tonazzo. Neutron background - could it be due to near miss muons? Presentation at Double Chooz Collaboration Meeting 2005.

[40] Guillaume Mention, Thierry Lasserre, and Dario Motta. A unified analysis of the reactor neutrino program towards the measurement of the θ_{13} mixing angle. 2007.

[41] Technical board members. Double chooz technical design report draft v1.0. 2007.

[42] A. Tonazzo. The double chooz detector. available at http://doublechooz.in2p3.fr.

[43] Double chooz collaboration website. http://doublechooz.in2p3.fr.

[44] G. Horton-Smith. An introduction to glg4sim features. http://neutrino.phys.ksu.edu/∼GLG4sim/GLG4sim-intro-2006-05-19.pdf, May 2006.

[45] Geant4 Collaboration. Introduction to geant4. http://geant4.web.cern.ch, June 2007.

[46] Root user's guide v5.16. http://root.cern.ch/root/doc/RootDoc.html, July 2007.

[47] Alfred Tang, Glenn Horton-Smith, Vitaly A. Kudryavtsev, and Alessandra Tonazzo. Muon simulations for super-kamiokande, kamland and chooz. *Phys. Rev.*, D74:053007, 2006.

[48] P. Antonioli, C. Ghetti, E. V. Korolkova, V. A. Kudryavtsev, and G. Sartorelli. A three-dimensional code for muon propagation through the rock: Music. *Astropart. Phys.*, 7:357–368, 1997.

[49] Dimitri Denisov. Detection of muons. http://www-ppd.fnal.gov/EPPOffice-w/Academic_Lectures/Denisov_%20Lecture.pdf, 2000. Academic lecture @ Fermilab.

[50] C. Grupen, Armin Boehrer, and L. Smolik. Particle detectors. *Camb. Monogr. Part. Phys. Nucl. Phys. Cosmol.*, 5:1–455, 1996.

[51] M.J. Berger and S.M. Seltzer. Tables of energy losses and ranges of electrons and positrons. *National Aeronautics and Space Adminnistration Report NASA-SP-3012, Washington DC*, 1964.

[52] Michael F. Ashby and David R. Jones. Engineering materials 2, with corrections (in english). Oxford: Pergamon Press. ISBN 0-08-032532-7;(1986).

[53] D. Greiner, private communication.

[54] F. Elisei et al. Measurements of liquid scintillator properties for the borexino detector. *Nucl. Instrum. Meth.*, A400:53–68, 1997.

[55] David Reyna. Design development for the outer veto. http://doublechooz.in2p3.fr/RestrictedArea/Meetings/chooz_06_2005 /Friday/Veto/Reyna_DC_10June2005_OuterVeto.ppt, 2005. Presentation for DoubleChooz Collaboration.

Versicherung und Einverständniserkläung zur Veröffentlichung

Hiermit versichere ich, dass ich die vorliegende Diplomarbeit selbstständig und ausschließlich mit den angegebenen Quellen verfasst habe. Ferner erkläre ich mich mit der Bereitstellung der vorliegenden Diplomarbeit in den Bibliotheken des Instituts für Experimentalphysik und des Fachbereichs Physik der Universität Hamburg einverstanden.

Hamburg im Februar 2008

Thorsten Lammers